Journal Pre-proof

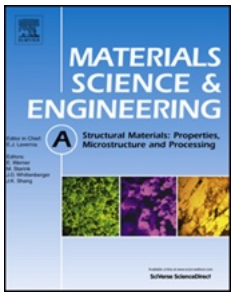

Hybridisation of microstructures from three classes of titanium alloys

Ahmad Zafari, Edward W. Lui, Shenbao Jin, Mogeng Li, Tesfaye T. Molla, Gang Sha, Kenong Xia

PII: S0921-5093(20)30650-X

DOI: https://doi.org/10.1016/j.msea.2020.139572

Reference: MSA 139572

To appear in: *Materials Science & Engineering A*

Received Date: 30 March 2020

Revised Date: 12 May 2020

Accepted Date: 12 May 2020

Please cite this article as: A. Zafari, E.W. Lui, S. Jin, M. Li, T.T. Molla, G. Sha, K. Xia, Hybridisation of microstructures from three classes of titanium alloys, *Materials Science & Engineering A* (2020), doi: https://doi.org/10.1016/j.msea.2020.139572.

This is a PDF file of an article that has undergone enhancements after acceptance, such as the addition of a cover page and metadata, and formatting for readability, but it is not yet the definitive version of record. This version will undergo additional copyediting, typesetting and review before it is published in its final form, but we are providing this version to give early visibility of the article. Please note that, during the production process, errors may be discovered which could affect the content, and all legal disclaimers that apply to the journal pertain.

© 2020 Published by Elsevier B.V.

Journal Pre-proof

Ahmad Zafari: Conceptualization, Methodology, Formal Analysis, Investigation, Writing-Original Draft, Funding Acquisition. **Edward W. Lui:** Investigation. **Shenbao Jin:** Investigation. **Mogeng Li:** Visualization, Formal analysis, Software. **Tesfaye T. Molla:** Software. **Gang Sha:** Investigation. **Kenong Xia:** Supervision, Conceptualization, Writing-Review & Editing, Funding Acquisition.

Journal Pre-proof

Journal Pre-proof

Hybridisation of microstructures from three classes of titanium alloys

Ahmad Zafari[a]*, Edward W. Lui[a,b], Shenbao Jin[c], Mogeng Li[a], Tesfaye T. Molla[a], Gang Sha[c], Kenong Xia[a]*

[a] *Department of Mechanical Engineering, The University of Melbourne, Victoria 3010, Australia*

[b] *Centre for Additive Manufacturing, School of Engineering, RMIT University, Victoria 3000, Australia*

[c] *School of Materials Science and Engineering, Herbert Gleiter Institute of Nanoscience, Nanjing University of Science and Technology, Nanjing, 210094, China*

***Corresponding authors (Email):** zafari.a@unimelb.edu.au; k.xia@unimelb.edu.au

Journal Pre-proof

Abstract

A ternary hybrid Ti alloy (HYTA) was produced by selective laser melting (SLM), combining all three classes of the titanium system. The hybridisation of the α CP Ti, α-β Ti-64 and β Ti-5553 gave rise to a highly heterogeneous microstructure encompassing all the possible phases and structures which do not co-exist in conventional monolithic Ti alloys. The details of the complex microstructure were comprehensively characterised, revealing the roles played by such important factors as the distribution of the ingredient alloy particles, the Marangoni convection and diffusion of solute during melting, and microsegregation of solute during solidification. The ternary HYTA exhibited an excellent combination of high tensile yield strength of 1000 MPa and enhanced ductility with uniform elongation of ~15% and total elongation of ~20%, superior to conventional Ti alloys of various types. Such exceptional performance is attributed to the high-degree

Journal Pre-proof

heterogeneity and the operation of most major deformation mechanisms which coordinate effectively and transfer smoothly between various parts with a wide range of hardness (4–6 GPa). The outcome has further demonstrated the potential of hybridisation of microstructures as a new strategy for future alloy development.

Keywords: Titanium alloys, hybrid alloys, uniform elongation, multiphase, selective laser melting.

Journal Pre-proof

Journal Pre-proof

1. Introduction

Nature has provided inspirations for engineering materials for a long time, typically by hybridising organic and ceramic structures in a sophisticated way to deliver unique properties. Such complex organisations, however, are hard to realise in metals. The advanced high strength steel (AHSS) comes close with its versatile phase structures and deformation mechanisms, including twinning induced plasticity (TWIP) and transformation induced plasticity (TRIP) [1]. Most of the other alloy systems are not as blessed. Titanium, with its three main classes of alloys, namely α, α-β, and β with the first two dominated by hcp-structured α and the latter by bcc β [2], can offer a wide variety of structures including pure β, lath and acicular hcp martensitic α', orthorhombic martensitic α'' and lamellar α/β. However, the various microstructures cannot co-exist through conventional processing (e.g. upon quenching single β is only achievable in β Ti while martensitic α' only in α or α-β Ti) [2]. One consequence is that most high strength Ti alloys lack ductility, especially uniform elongation (UE) which is desirable in many manufacturing processes. In particular, two of the most used structural alloys, Ti-6Al-4V (Ti-64) and Ti-5Al-5V-5Mo-3Cr (Ti-5553), showed low work hardening, leading to UE of < 6% with strength increased above 1000 MPa [3]. Although TWIP and TRIP in some β alloys designed by the *d*-electron method can improve ductility, their yield strengths (YS) are normally as low as 500-800 MPa [4, 5]. Similarly, a dual phase α/α' Ti-64 produced using the costly elaborative processing of electron beam melting (EBM), hot isostatic pressing (HIP) and heat treatment exhibited low UE of 4% when YS was raised to > 1000 MPa [6].

In our recent study [3], we have employed selective laser melting (SLM) to create a novel Ti by hybridising microstructures from existing Ti alloys, referred to as HYbrid Ti Alloy (HYTA), achieving an excellent combination of strength and ductility. This strategy is different from the common practice of mixing elemental powders for in-situ alloying with a view to fabricating a homogeneous structure or producing a simple metal matrix composite [7-10]. Instead, a

Journal Pre-proof

heterogeneous microstructure combining that of Ti-5553 (dominated by β) and that of Ti-64 (α'), which do not coexist in conventional alloys, has been obtained in HYTA. This leads to an exceptionally high work hardening rate, UE of 10-13%, total elongation (ε_t) of ~15% and ultimate tensile strength (UTS) of ~1200-1300 MPa. Further, Ti-5553 and Ti-64 can be selectively manipulated using heat treatments to improve ε_t to ~20% or YS to 1100 MPa [3].

However, compositional interactions between the ingredient alloys, which has not been investigated before, deserve special attention to understand how HYTA forms and behaves. Several important factors must be considered in the formation of the hybrid microstructure. First, convection may have played an important role since it would create layers of the ingredient alloys in the melt pool. Such layered structures also formed during AM of elemental powders [11], but were ignored since the aim there was to eliminate them and produce homogeneous structures. Second, different sizes and masses of solute atoms would result in different diffusion rates [12], affecting their distribution. Third, different partition coefficients (k) upon solidification would change the composition of the solidifying liquid, causing microsegregation. Hence, a more in-depth study is essential to reveal the roles played by these factors in the final microstructure of HYTA.

On the other hand, the good mechanical properties in the binary HYTA has been attributed to the effective deformation transfer and coordination between the α-β Ti-64 and β Ti-5553 [3]. It appears desirable and of significant interest to add an α type alloy to produce a ternary HYTA with a view to generating a more sophisticated hybridisation of the microstructures covering all the possible phases/structures in the Ti system. It is expected that further property enhancement can be achieved.

Here we report the successful production by SLM of a new ternary HYTA with commercially pure (CP) Ti of α type added as the third ingredient to the binary Ti-64 (α-β) and Ti-

Journal Pre-proof

5553 (β), focusing on the interactions between the three alloys in the melt pool as well as the resulting tensile properties and deformation mechanisms. A strong influence on CP Ti by the other two alloys was observed while the interaction between Ti-64 and Ti-5553 was limited. Most common phases and structures from all three types of Ti alloys were seen to co-exist in the ternary HYTA, leading to an improved combination of strength and ductility compared to the binary one, with YS of ~1000 MPa, UTS of ~1100 MPa, UE of 15%, and ε_t of ~20%. These excellent results serve as further proof that the new strategy of hybridising microstructures is promising for future alloy development to achieve unique and exceptional performances in metals.

2. Experimental Materials and Procedures

A ternary HYTA was produced by mixing equal portions (~33 wt.%) of plasma atomised CP Ti (Grade 2), Ti-64 and Ti-5553 powders (15–45 μm and distribution of D10 = 22 μm, D50 = 35 μm and D90 = 46 μm) using a mechanical stirrer at 300 rpm. The Renishaw AM250 SLM system was employed for printing rods of 8 mm in diameter and 52 mm in height using stripe scanning strategy on a titanium substrate at room temperature in an atmosphere set at 100 ppm oxygen. The time between two successive depositions (interlayer time) was ~30 s. Other parameters are listed in Table 1. For comparison, a binary HYTA consisting of 50 wt.% Ti-64 and 50 wt.% Ti-5553 was also produced under the same conditions. Nearly full density of > 99.4% was achieved.

Table 1 Main printing parameters used.

Stripe size (mm)	Layer thickness (μm)	Point distance (μm)	Exposure time (μs)	Power (W)	Hatch spacing (mm)	Laser spot size (μm)	Rotation angle between layers (°)
5	30	45	50	200	0.105	66	67

Journal Pre-proof

The distribution of the ingredient alloys before and after SLM was constructed using WDS/EDS elemental maps. The intensity data for Mo, Al and Ti were analysed using MATLAB with the high intensity areas distinguished by setting an empirical threshold of ~70%, i.e. regions with high Mo intensity (i.e. greater than the threshold) identified as Ti-5553 (only Ti-5553 contained Mo), those with high Al intensity but no Mo as Ti-64, and those with Ti only as CP Ti.

Microstructures were characterised by scanning electron microscopy (SEM, FEI Teneo), and transmission electron microscopy (TEM, FEI Tecnai F20). Backscattered electron (BSE) imaging was performed using analytical mode at an accelerating voltage of 10 keV and current of 13 nA. TEM samples were cut using focused ion beam (SEM/FIB, FEI Nova 200 Nanolab DualBeam). The in-situ lift out FIB technique produced foils of ~2 μm thick which were thinned by milling at 30 keV, resulting in foils of < ~100 nm in thickness after removing contaminations deposited on the surfaces by milling at a lower voltage of 10 keV. Electron probe microanalyser (EPMA, JEOL JXA-8530F) was employed for WDS/EDS analyses using a voltage of 15 keV, dwell time of 50 ms and step size of 1 μm. Further compositional analysis was conducted using atom probe tomography (APT) in a local electrode atom probe (LEAP 4000X Si) at a UV laser pulse repetition rate of 200 kHz, energy of 70 pJ, target evaporation rate of 0.5% and specimen temperature of 50 K.

Tensile specimens with a gauge size of 4 mm in diameter and 16 mm in length were cut from the printed rods. The gauge was in the middle section of the rod and the top and bottom layers were not included. The tensile tests were conducted with loading parallel to the build direction at an initial strain rate of 2.5×10^{-4} s^{-1} according to ASTM E8/E8M-13. A laser extensometer (MTS LX500) was used to accurately measure strain.

Nanoindentation was performed on mirror polished surface using a Hysitron TI950 Triboindenter equipped with a Berkovich pyramidal-shaped indenter tip. Hardness mapping across

Journal Pre-proof

an area of 70 × 300 μm^2 was performed with spacings of 4 μm between indents, peak load of 10 mN and loading/unloading rate of 1 mN/s. The nanoindentation results were analysed using TriboScan and visualised using MATLAB.

3. Results

3.1. As-mixed powders

The binary mixed powder of Ti-64 and Ti-5553 was characterised by the Mo EDS elemental map shown in Fig. 1a. Since Mo only existed in Ti-5553, its intensity was used to distinguish Ti-5553 particles from the Ti-64 ones, resulting in the binary distribution of red (Ti-5553) and blue (Ti-64) in Fig. 1b. Rather than individual particles, clusters of ~100-200 μm of each ingredient alloy (selectively circled) formed.

For the ternary mixed powder of CP Ti, Ti-64 and Ti-5553, the Ti, Al and Mo EDS elemental maps are shown in Figs. 1c-e, respectively. The CP Ti particles are those with higher intensity of Ti but free of Al and Mo, Ti-5553 particles are the ones containing both Mo and Al, and Ti-64 particles contain Al without Mo. Quantitative intensity analyses led to the identification of CP Ti particles as yellow, Ti-64 blue and Ti-5553 red in Fig. 1f (this colour scheme is used hereinafter). Compared to Fig. 1b, all three types of clusters are much smaller than 100 μm although a small number of clusters of the order of 100 μm (selectively circled in Fig. 1f) are present.

3.2. As-SLM microstructures

Fig. 2a shows BS-SEM of the as-SLM ternary HYTA, revealing the columnar prior β grains (selectively shown by white dotted lines) from epitaxial growth and the dark and bright layers in the melt pool (selectively delineated by yellow dashed lines) with the former containing acicular

Journal Pre-proof

martensitic α' plates and the latter β grains confirmed later by high magnification SEM and TEM. The contrast between the layers was resulted from different distributions of heavier and lighter solute atoms, as revealed by WDS elemental mapping in Figs. 2b-g (not very obvious for Cr and Fe because of their much smaller amounts – maximum 3 wt.% Cr and 0.5 wt.% Fe). The three ingredient alloys were identified using similar intensity analyses to those for the as-mixed powders and colour rendered in Fig. 2h. Indeed, WDS/EDS point analyses (not shown here) confirmed their compositions to be close to the nominal ones of the ingredient alloys. It is, however, noted that a significant area in Fig. 2h cannot be associated with any of the ingredient alloys (marked as black). In other words, the black region possesses compositions different from the ingredient alloys. Consequently, the amount of each ingredient alloy was reduced, compared to the as-mixed powder (Fig. 1f), especially for the CP Ti.

Closeups of the ternary HYTA are shown in Figs. 3a-d with chemical compositions from WDS analysis at points 1-9 listed in Table 2. In sufficiently thick layers of > ~5-10 μm (Figs. 3a-b) the original compositions of the ingredient alloys are preserved, i.e. points 1 and 4 as Ti-5553, 2 and 5 as Ti-64, and 3 as CP Ti. In contrast, thin layers of < ~1-2 μm were turned into new alloys. For example, points 6 and 7 contained a high amount of Mo and V, indicating their origination from Ti-5553. However, the contents of the β stabilising elements were much lower than Ti-5553, suggesting that these thin layers had been diluted into a new α-β Ti alloy not stable enough to prevent the formation of needle-shaped martensitic plates (bottom, Fig. 3c). In fact, such a deviation from the ingredient alloy composition occurred even at the boundary of the thick layers (~1 μm in thickness as yellow arrowed in Fig. 3b), reducing β stability and allowing martensitic transformation (inset in Fig. 3b). In addition to the layered structures, there were some isolated regions of single phase acicular α', as shown in Fig. 3d, with compositions different from those of the ingredient alloys (e.g. points 8 and 9). For comparison, the as-SLM binary HYTA shown in Fig. 3e contained mostly thick layers of > 10-20 μm with largely unchanged compositions, resulting in

Journal Pre-proof

single β in the Ti-5553 region and α' in the Ti-64 region. In some cases, as selectively delineated by dotted lines in Fig. 3e, the melt pools were entirely occupied by either of the alloys, creating blocks of Ti-5553 (β) and Ti-64 (α').

Table 2 Contents of solute elements (wt.%) at the points numbered 1 to 9 in Fig. 3.

Element	1	2	3	4	5	6	7	8	9	Ti-64	Ti-5553
Al	4.72	6.05	-	4.4	5.6	3.89	3.53	4.94	4.58	5.5-6.5	4.4-5.7
V	4.94	3.8	-	4.8	3.5	3.45	3.36	3.87	2.56	3.5-4.5	4-5.5
Mo	5.27	-	-	5.21	-	1.97	2.67	-	1.72	-	4-5.5
Cr	2.61	-	-	2.88	-	1.07	1.34	-	0.75	-	2.5-3.5
Fe	0.32	-	-	0.27	-	0.17	0.27	-	0.2	<0.25	0.3-0.5

The martensitic α' formed in the newly created alloy regions (e.g. Fig. 3d) was further studied using TEM. Acicular α' typical in α-β Ti alloys was observed (Fig. 4a). The α' plates, in particular large ones, were twinned (arrowed) with the twin planes identified to be of $\{0\bar{1}1\bar{1}\}$ type based on the SAEDP (Fig. 4b) from the circled spot in Fig. 4a. This twinning is often observed in acicular martensite formed upon rapid cooling from the β field [13, 14]. Additionally, dislocations (selectively arrowed in Figs. 4c and d) and stacking domains (Fig. 4e) were observed. Although substructural dislocations and twins have been widely observed, the stacking domains have been reported only once before [15], which are attributed to atom shuffling as an essential mechanism of the bcc to hcp martensitic transformation.

To shed light on the interaction between the ingredient alloys, the interfacial area between the ingredient alloys was investigated. One interface between CP Ti and Ti-5553 (dashed line) is shown in Fig. 5a together with the corresponding Al, Mo, V and Ti elemental maps. The higher concentrations of Al and Mo (brighter contrast) below the dashed line and the higher concentration

Journal Pre-proof

of Ti above it identify the area below as initially Ti-5553 and above as originally CP Ti. The boundary is, however, no longer sharp, with significant amount of alloying elements in Ti-5553 penetrating into the original Ti region (a composition of ~2 wt.% V, ~1.5 wt.% Al, 1 wt.% Mo and < 1 wt.% Cr was revealed by point EDS analysis above the dashed line). It is apparent that V was almost uniformly distributed across the original interface but there were still higher amounts of Al and Mo on the Ti-5553 side despite their penetration into Ti. The changes in composition across the interface led to the formation of acicular martensitic plates in both regions.

More detailed characterisation was performed using TEM at such an interface, as shown in Fig. 5b-h. Four main zones were identified, as delineated by dashed lines and labelled A-D in Fig. 5b. SAEDP from A is shown in Fig. 5c and DF for $(110)_\beta$ in Fig. 5d, both indicating single β phase in A, i.e. Ti-5553. By slight tilting, substructural dislocations in D was observed (Fig. 5e), as typically seen in martensitic α' in CP Ti or diluted Ti alloys. SAEDP from Zone B is shown in Fig. 5f, identifying the martensitic plates observed to be orthorhombic α'' twinned on $(1\bar{1}1)$. However, the structure in Zone C looked more like acicular α' seen in Fig. 4a, as confirmed by SAEDP in Fig. 5g taken from multiple α' plates. The STEM-EDS elemental maps for the red-dot framed region in Fig. 5b are shown in Fig. 5h. The Al and V maps revealed higher intensity of both elements in B than A, although V showed a more significant difference. On the other hand, Cr and particularly Mo were higher towards A. Hence, Ti-5553 was slightly depleted of Al and more significantly of V, but enriched mainly in Mo, consistent with the elemental maps in Fig. 5a and point WDS/EDS analyses.

The interface between CP Ti and Ti-64 was hard to find since Ti would obtain the same acicular α' microstructure as Ti-64 after SLM (Fig. 4). The interaction of Ti with Ti-64 is, however, expected to be like that with Ti-5553 since they contain similar amounts of Al and V. On the other hand, the interaction between the Ti-64 and Ti-5553 was much more limited, as point WDS/EDS analyses on adjacent Ti-64/Ti-5553 layers revealed almost no change in their compositions except

Journal Pre-proof

for regions very close to the interfaces or very thin Ti-64 and Ti-5553 layers (Fig. 3, Table 2 and Ref. [3]). In general, a large number of WDS/EDS point analyses in those regions altered from the original ingredient alloys revealed compositions of ~2-3 wt.% V, ~2-3 wt.% Al and <1-2 wt.% Mo and Cr, indicating that V and Al were the main solute elements responsible for the composition change during SLM.

3.3. Internal cells in Ti-5553

Fig. 6a shows internal cells in the Ti-5553 regions of HYTA revealed after chemical etching. The formation of such cells in Ti-5553 is attributed to the effect of constitutional supercooling on the geometry of growth during solidification [16]. However, it is not known how solute elements are distributed in front of the solid/liquid interface to create such supercooling. This is particularly important in HYTA, since microsegregation of solute elements would affect the surrounding solidifying liquids from other ingredient alloys, leading to various microstructures. APT was performed on an as-SLM single Ti-5553 alloy to avoid complications in HYTA. This was justified since the cells were only found in thick Ti-5553 layers in HYTA which were not affected by the other ingredient alloys. Pre-APT SEM of the as-SLM Ti-5553 is shown in Fig. 6b, revealing the locations of the melt pool boundaries and fine cells. Single atom maps for various elements from an area inside a melt pool and in its boundary are shown in Figs. 6c and d, respectively. Visual inspection appeared to suggest that all the elements were uniformly distributed in both regions. Quantitative distribution of the elements other than Mo as a function of the distance from the boundary confirmed this observation (Fig. 6e). Mo, however, tended to enrich in the melt pool boundary. In particular, the concentration of Mo at the boundary (distance 0 in Fig. 6e) was ~6 at.% which gradually reduced to ~4 at.% inside the melt pool. The average chemical compositions inside the melt pool and in the boundary are listed in Table 3, confirming the most significant difference in Mo of ~1 at.%.

Journal Pre-proof

Table 3 Average chemical compositions inside the melt pool (MP) and in the melt pool boundary (MPB) analysed by APT.

		Ti	Al	V	Mo	Cr	O	Fe	N	Si	C
MP	**at.%**	80.8	8.15	4.60	3.21	2.35	0.43	0.30	0.09	0.05	0.005
	wt.%	80.94	4.60	4.90	6.45	2.56	0.14	0.35	0.03	0.03	~0.00
MPB	**at.%**	80.4	8.29	4.35	4.21	1.99	0.45	0.17	0.07	0.02	0.006
	wt.%	79.85	4.64	4.60	8.38	2.15	0.15	0.2	0.02	0.01	~0.00

3.4. Hardness distribution and tensile properties

Fig. 7a shows the hardness map obtained from nanoindentation along the build direction, and the WDS elemental maps of Ti, Al and Mo are shown in Figs. 7b-d, respectively. The same method used for the production of Fig. 2h was employed to construct the distribution of the ingredient alloys as well as the altered regions from the elemental maps, as shown in Fig. 7e. The white dots with white contour in Fig. 7e represent hardness data points of > 5.2 GPa in Fig. 7a, associated with α' with high contents of solute elements (e.g. Ti-64). On the other end of the hardness spectrum, the green dots with green contour indicate regions of < 4.5 GPa, related to areas largely free of acicular α' (e.g. Ti-5553 and CP Ti). The vast majority of the area exhibited hardness values between these two limits. In general, the distribution of hardness is very heterogeneous thanks to hybridisation.

Fig. 7f shows the tensile engineering stress-strain curves for the binary and ternary HYTAs as well as ingredient alloys together with derived properties. The ternary HYTA exhibited much higher YS of ~1000 MPa, ε_t of ~20%, and UE of ~15%, compared to YS of ~750 MPa, ε_t of ~14%, and UE of ~11% for the binary HYTA. Although the monolithic Ti-64 showed higher strength as a result of the higher amount of Ti-64 (the hardest ingredient alloy), its UE of ~5% was significantly

Journal Pre-proof

lower compared to both HYTAs, and ε_t of ~14% was much inferior to 20% for the ternary HYTA. While ε_t for Ti-5553 and CP Ti were comparable to that for the ternary HYTA, their strengths were considerably lower by > 200 MPa.

The work hardening rate for the binary and ternary HYTAs, calculated as $d\sigma/d\epsilon$ with σ and ϵ as true stress and true strain, respectively, is shown in Fig. 7g, displaying much higher values in the binary HYTA at $\epsilon > 5\%$. The calculated UE using the criterion $d\sigma/d\epsilon = \sigma$ gave rise to 11-12% for the binary and 14-15% for the ternary, consistent with the values obtained from the engineering stress and strain curves (Fig. 7f).

3.5. Microstructures after tensile deformation

The deformation structures after tensile straining to ~1.5% are shown for the binary (Fig. 8a) and ternary (Figs. 8b-j) HYTA. Slip bands were present in both although their number was higher and spacing smaller in the ternary HYTA (Figs. 8a and b). In addition to dislocation slip, lens-shaped plates were formed in the β region of the ternary HYTA (STEM-HAADF in Fig. 8c), identified as stress induced martensitic α" using the inset SAEDP which also revealed diffraction from athermal ω (ω_{ath}). Although most of the strain was accommodated in β, dislocations were also generated in α' (yellow triangles) near the α'/β interface (dashed-line), as shown in Fig. 8d. At some α'/β interface, rotation of β crystal can be observed in a thin band (separated by dashed lines) in Fig. 8e, as proven by SAEDPs in Figs. 8f-h corresponding to areas *f*, *g* and *h* in Fig. 8e. In particular, Fig. 8f confirms area *f* as β. When diffraction was taken from *g* which crossed the dashed line, extra spots in addition to those identified in Fig. 8f (pointed by triangles) were present, forming the pattern shown by solid lines (Fig. 8g). This new pattern turned out to be the same as that shown in Fig. 8h taken from location *h* in Fig. 8e (i.e. entirely within the thin band) and was indexed as β. In other words, both areas *f* and *h* are β but with different orientations. DF from the circled spot in Fig.

Journal Pre-proof

8g confirmed the presence of crystals with different orientations in area *h* (Fig. 8i). The lens-shaped martensitic plates found in area *h* (Fig. 8j) was identified to be α" using the corresponding SAEDP (inset) as well as the DF.

Further straining to 6.5% led to the formation of more slip bands and dislocation pileups at the α'/β interface in the ternary HYTA (Fig. 9a). At another location, Fig. 9b shows a thin stripe delineated by dashed lines sandwiched between two Ti-5553 regions. Chemical analysis showed that the contents of β stabilising elements in this area were slightly lower than in Ti-5553. The plates observed in this region were identified as martensitic α" using electron diffraction (not shown here). The interaction between slip bands and α" created dislocation pileups (Fig. 9b). DF TEM for α" in Fig. 9c shows that some of the slip bands (selectively shown by dashed lines) were able to cut through the martensitic plates to create square-shaped α", as seen in a commercial β Ti-5553 [17].

At tensile fracture, steps at the α'/β interfaces (shown by dashed lines) were formed (Fig. 9d), aligned with slip bands (selectively shown by yellow dotted lines). Tilting the sample revealed that the steps were able to penetrate into α' by creating slip bands, as arrowed in Fig. 9e. Dislocation pileups at α'/β interfaces could trigger twinning in the entire layer of a diluted Ti alloy (Fig. 9f), identified as $\{10\bar{1}1\}$ type using the inset SAEDP. The red dotted line in Fig. 9f distinguishes two β regions with different orientations from crystal rotation, similar to observation in Fig. 8e. Fig. 9f also shows dislocation pileups at both β/β (red dotted line) and α'/β interfaces. The former can be seen more clearly using STEM-HAADF in Fig. 9g.

Journal Pre-proof

Journal Pre-proof

4. Discussion

Hybridisation of microstructures from different alloys promises to offer new opportunities for materials development by providing exceptional performances not possible in individual ingredient alloys. SLM is shown to be most potent in producing hybrid alloys thanks to ultrahigh cooling rates (> 10^6 K/s) which largely preserves the identities of the ingredient alloys. The first type of such materials was successfully realised from SLM of pre-alloyed Ti-64 and Ti-5553 powders, leading to a binary HYTA with excellent mechanical properties [3]. In the present work, a third alloy, CP Ti of α type, was added to the α/β and β types to make a ternary HYTA encompassing all possible phases and structures in the Ti system. The resulting microstructure turns out to be much more complex, compared to that of the binary HYTA, leading to improved tensile properties. Several important factors involved in SLM processing such as the distribution and proportion of ingredient powders, convection in the melt pool, diffusion in liquid and micro-segregation need to be studied to understand their roles in the formation of the sophisticated microstructure. It is also critical to understand the fundamentals responsible for the excellent mechanical properties in the ternary HYTA.

4.1. Effects of convection, diffusion and microsegregation

Convection

The schematics in Fig. 10 show the formation of the final microstructures in one melt pool (of the order of 100 μm in size) in the binary (rows a, b and c) and ternary (row d) HYTAs. Column 1 displays the possible distributions of the pre-alloyed powders of Ti-64 (blue), Ti-5553 (red) and Ti (yellow). Column 2 shows the distributions of the alloys after melting, formed by the Marangoni convection (illustrated at the bottom) resulting from a steep thermal gradient in the melt pool [18]. Column 3 illustrates the microstructures immediately upon solidification, exhibiting prior

Journal Pre-proof

β grain boundaries (white lines) and alloy distributions unchanged from column 2. Column 4 represents the final microstructures after quenching to low temperatures.

In the binary HYTA, many of the clusters of Ti-64 and Ti-5553 are <~100 μm in size (Fig. 1b), filling the melt pool as in Fig. 10a1, although some clusters are as large as ~200 μm, resulting in the entire melt pool being occupied by either alloy (Figs. 10b1 and c1). When there are two alloys in the melt pool, the Marangoni convection would create liquid layers of the alloys (Fig. 10a2) and significant mechanical mixing, which could result in one uniform composition in the whole melt pool, is prevented by the ultrahigh cooling rates during SLM (i.e. > 10^6 K/s). Following rapid solidification, prior β columns are formed in both but the shape and distribution of the alloy layers are unchanged (Fig. 10a3). The original composition of each ingredient alloy (i.e. Ti-64 or Ti-5553) is largely preserved although some dilution could occur at the Ti-64/Ti-5553 interface [3]. Since the ingredient alloys have similar melting points and both solidify into β below the solidus temperatures, perfect fusion between particles is achieved in HYTA with density of > 99.4%. The internal cells formed in Ti-5553 (Fig. 6a) are represented by the black lines in Figs. 10a3 and c3 (discuss later). Quenching to low temperatures transforms the Ti-64 layers (blue) into acicular martensitic α', but high contents of β stabilising elements in Ti-5553 (red) suppress any martensitic transformations (Fig. 10a4). In the cases of single occupations (Figs. 10b1 and c1), there is only one alloy in the melt pool, resulting in either a Ti-64 (Fig. 10b4) or a Ti-5553 (Fig. 10c4) microstructure, as observed in Fig. 3e.

The clusters in the ternary HYTA are considerably smaller (Fig. 1f) and most melt pools would contain all three alloys (Fig. 10d1), making the microstructure more complicated since layers created by the convection can have a wide range of thicknesses (Fig. 10d2 and observed in Figs. 3a-d) and in most cases smaller than those in the binary HYTA. The inside of the relatively thick layers (> ~5-10 μm) can maintain the original compositions, but the entire thinner ones (< ~1-2 μm) as

Journal Pre-proof

well as a thin layer at the interface of the thick layers would undergo compositional changes (Table 2). These layers with altered compositions are represented by orange in Fig. 10d2, taking into consideration that CP Ti is affected considerably more than the other two alloys (Fig. 2h). The compositions of the orange layers fall in the range of the α-β Ti alloys (Table 2, WDS/EDS point analyses and elemental maps presented in 3.2), as shaded in the schematic phase diagram in Fig. 11a. Therefore, after quenching to low temperatures, these orange layers with new compositions would also transform into acicular α' (Fig. 10d4 as observed in Figs. 4 and 5). The much smaller amount of remaining CP Ti would undergo β to massive martensitic α' transformation [2], creating large α' plates with substructural dislocations (Figs. 5b and e). Although overlapping melt pools in one track and two consecutive layers deposited could lead to further mixing and diffusion, the effects on the overall microstructure as described here are minimal. Additionally, the low temperature of the substrate and long interlayer time (~30 s) minimised the heat accumulation during SLM, resulting in the precipitation of only a small amount of α in isolated regions in the bottom layers.

Diffusion in the liquid state

Convection includes two main sub-mechanisms of advection (directional bulk flow transfer of heat, in which the Marangoni effect falls) and diffusion (non-directional transfer of mass particles stemmed from a concentration gradient). The Marangoni convection has been identified as the cause for forming the alloy layers but not for altering the alloy compositions in the thin layers and at the interface. It is time to ask what mechanisms are responsible for it and why CP Ti is affected more than the other two alloys. It is recalled that V and Al are the main elements responsible for the changing compositions. For example, Figs. 5a and h clearly show rejection of V and Al from Ti-5553, leaving Mo behind. This confirms that the convection (refers to the sub-mechanism advection) is not the reason since it would not selectively reject or enrich any particular

Journal Pre-proof

elements. Instead, solute diffusion in the liquid state and microsegregation should be considered. The diffusion coefficient of solute *x* in liquid Ti ($D_{x\,Ti}$) can be calculated using [12]

$$D_{x\,Ti} = \frac{0.002628\sqrt{T^3[m_x+m_{Ti}]/2m_x m_{Ti}}}{p d_{x\,Ti}^2 \Omega_{x\,Ti}^{(x,x)*}(T_{x\,Ti}^*)} \quad (1)$$

where *p* denotes pressure in atmospheres, *T* temperature (K), $d_{x\,Ti}$ the average atomic diameters of *x* and Ti (i.e. $d_{x\,Ti} = \frac{(d_x+d_{Ti})}{2}$), m_x and m_{Ti} the atomic masses of *x* and Ti, respectively, and $\Omega_{x\,Ti}^{(x,x)*}(T_{x\,Ti}^*)$ the collision integral taken as unity for rigid spheres. At a given temperature, the atomic size and mass of the solute element determine its diffusivity in liquid Ti. Table 4 lists $d_{x\,Ti}$ and $[m_x + m_{Ti}]/2m_x m_{Ti}$ calculated for the four main solute elements of V, Al, Cr and Mo in the ternary HYTA. Al diffuses faster than all the other elements and Mo is the slowest, while Cr and V diffuse at the same rate between Al and Mo. The diffusion coefficients calculated for Ti-*x* (*x* = V, Al, Mo or Cr) at the temperature range of 1600-2000 °C (i.e. in liquid) using CALPHAD are shown in Fig. 11b, confirming that Mo diffuses at a much slower speed. The faster diffusion of Al and V allows them to move into the neighbouring layer in much shorter times and to play more important roles in compositional changes. Although Cr can diffuse as fast, its concentration is lower, making it less visible.

Table 4 The atomic diameter (d_x) and mass (m_x), $M_{x\,Ti} = [m_x + m_{Ti}]/2m_x m_{Ti}$ and $d_{x\,Ti}$ for solute *x* (= Al, V, Mo or Cr) in Ti, giving rise to $D_{x\,Ti}/D_{Al\,Ti}$ denoting the diffusion coefficient of *x* in liquid Ti normalised by that of Al.

Element	d_x (pm)	m_x (u)	$M_{x\,Ti}$	$d_{x\,Ti}^2$	$D_{x\,Ti}/D_{Al\,Ti}$
Ti	430	47.867	-	-	-
Al	286	26.981	0.0289	128164	1
V	410	50.941	0.02	176400	0.61
Mo	418	95.95	0.0.016	179776	0.52
Cr	400	51.996	0.02142	172225	0.62

Journal Pre-proof

In addition to diffusion coefficients, the amount of diffusion is also dependent on the concentration gradient of the solute element and this explains why the interaction between CP Ti and the other two alloys is more significant than that between Ti-5553 and Ti-64. CP Ti contains almost no solute elements and when coupled with Ti-64 or Ti-5553, which is rich in solute contents, a large concentration gradient is established for each solute element, providing a great driving force for its diffusion into CP Ti. At the same time, the concentration of Ti in CP Ti is higher than in Ti-64 and Ti-5553 by >10 and >18 wt.%, respectively, driving Ti to diffuse from CP Ti to the alloys. Consequently, Ti-64 and Ti-5553 are diluted into the range of α-β alloys, while CP Ti is enriched in solute elements so it also moves from the α to the α-β region (shaded in Fig. 11a). The formation of new α-β alloys is readily observed in the ternary HYTA, as typified in Figs. 3c-d, 4 and 5, and they exhibit a wide range of compositions. For example, in Zone *B* of Fig. 5b, which is very close to Ti-5553 (Zone *A*), the amount of β stabilising elements is less than that of Ti-5553, but still high to prevent any α' from forming upon quenching. Instead, the orthorhombic α" is formed (Fig. 5f). In other words, the local composition in *B* would be close to the α-β/β Ti boundary, as indicated by Alloy 1 in Fig. 11a. On the other hand, Zone *C* in Fig. 5b was closer to CP Ti (Zone *D*) with lower contents of β stabilising elements, creating an alloy closer to that of Ti-64 (e.g. Alloy 2 is in Fig. 11a), which undergoes β to acicular α' transformation.

Finally, it is worth noting that the diffusion length was apparently of the order of 1 μm since the composition changes only occurred in a slice (~1 μm) at the interface in the thick layers of > 5 μm but throughout the entire volume of the thin layers of < 1-2 μm.

Microsegregation and formation of internal cells

Microsegregation can influence the liquid composition in front of the solidifying alloy. No microsegregation is expected in Ti-64 since the partition coefficients (k) for V and Al are very close to unity [19]. Microsegregation in Ti-5553, however, is significant and might be responsible for the

Journal Pre-proof

formation of the internal cells (Figs. 6a-b). Such internal cells in as-SLM Ti-5553 was attributed to constitutional supercooling [16] although no compositional analysis was conducted to show which elements created the supercooling. The partition coefficients of V, Cr and Fe are smaller than unity (i.e. $k < 1$), making them depleted at the beginning of solidification and enriched towards the end while those of Al and Mo are larger than unity (i.e. $k > 1$), making them enriched at the start. During SLM, solidification starts at the melt pool boundary and consequently, Fe and Cr (with effective k of 0.6 and 0.8, respectively [20, 21]) are expected to be depleted and Mo and Al (with k of 1.41 and ~1.1-1.2, respectively [22, 23]) enriched at the boundary. Indeed, there are more Mo and Al and less Fe and Cr in the melt pool boundary based on APT results (Table 3). However, the most considerable segregation happens to Mo with its content ~1-2 at.% higher at the melt pool boundary whereas the segregation is less visible for the other elements (Table 3 and Fig. 6e). It is therefore concluded that the supercooling required for cellular growth is mostly provided by Mo microsegregation. Indeed, it was shown that adding Mo to Ti-64 could change its growth into cellular during SLM [23]. This can also be another factor affecting the composition of the solidifying liquid in the ternary HYTA. The enrichment of Mo in Ti-5553 reduces its amount in the surrounding liquid which eventually creates new α-β Ti with less Mo than Al and V.

4.2. Tensile behaviour

Table 5 compares tensile properties of the ternary HYTA to those of binary HYTA, monolithic Ti-64 and Ti-5553 which, besides being the ingredient alloys in HYTA, are two important commercial Ti alloys on their own right, and a range of TWIP/TRIP β Ti alloys whose high work hardenability owing to twinning and stress induced martensitic transformation (SIMT) has made them attractive. The data in Table 5 were all obtained from similar testing conditions (i.e. room temperature and quasi-static deformation), although not all followed ASTM E8. The ternary HYTA clearly exhibits an improved combination of strength and ductility. Compared to Ti-64, it

Journal Pre-proof

possesses similar YS of ~1000 MPa and UTS of ~1100 MPa but with substantially higher UE (~15%) and ε_t (~20%). Although the strength of Ti-5553 can be higher from precipitation hardening and total elongation reach ~18-20% (at a lower YS of 800 MPa though), its UE is in the range of 0-8% as a result of very small work hardening. The ternary HYTA is also superior to its binary counterpart with higher YS by 200-600 MPa, UE by 2-5% and ε_t by > 5%. As far as TWIP/TRIP β Ti alloys are concerned, they generally exhibit considerably lower strength with YS and UTS of 400-800 MPa and < 990 MPa, respectively, although ductility can be comparable or higher (when strength is at the lower end of the spectrum).

Table 5 Engineering yield strength (YS), ultimate tensile strength (UTS), uniform elongation (UE) and strain-to-fracture (ε_t) of ternary and binary HYTA, and Ti-64, Ti-5553, and TWIP/TRIP β Ti produced using different methods.

Alloy	YS (MPa)	UTS (MPa)	UE (%)	ε_t	Reference
Ternary HYTA	1000	1100	~15	20	Present work
Binary HYTA	750	1205	11	14	Present work
Binary HYTA	370	1200	11	18-20	[3]
Binary HYTA	1100	~1250	8	13-14	[3]
Binary HYTA	~800	~1250	13	15	[3]
Ti-64	790	870	< 6	18	[24]
Ti-64	990	1100	< 6	8	[24]
Ti-64	945	1070	~8	10	[25]
Ti-64	875-939	971-1192	4-10	4-12	[6]
Ti-64	1100	1200-1300	2-5	6-15	[26-28]
Ti-5553	800	800	0	18-20	[3]
Ti-5553	1245	1310	8	17	[29]
Ti-5553	1050-1220	1150-1300	< 8	4-10	[30]
TWIP/TRIP β Ti					
Ti-15Mo-5Zr	760	801	10	19	[31]
Ti-10Mo-2Fe	866	944	8	17	[31]
Ti-15Mo	439	714	27	49	[32]
Ti-15Mo-1Fe	837	837	0.2	20	[32]
Ti-10Mo-1Fe	563	825	24	43	[33]
Ti-10Mo-1Fe	626	833	24	32	[34]
Ti-20V-2Nb-2Zr	550-600	< 700	11-20	25-35	[35]
Ti-16V-1Fe	760	980	20	27	[36]

Journal Pre-proof

Ti-12V-2Fe-1Al	760	900	30	37	[36]
Ti-12V-2Fe-2Al	980	990	7	17	[36]
Ti-12Mo*	~500	~700	30	~48	[4]
Ti-8.5Cr-1.5Sn*	~550	~920	35	~40	[37]
Ti-18Zr-13Mo*	800	~900	18	18	[5]

* True stresses and strains given in the references converted to engineering.

As in the binary HYTA, plastic deformation starts in the softer Ti5553 in the ternary HYTA with the formation of slip bands (CP Ti is insignificant since its amount is much smaller as a result of solute element diffusion). However, the ternary HYTA yields at a higher stress of ~1000 MPa, as opposed to ~750 MPa for the binary one. First, this can be attributed to grain size strengthening. As discussed in 4.1, the β layers in the ternary HYTA are thinner than those in the binary one, shortening slip length in the former. Second, a higher number of the thinner β layers would be sandwiched between α' layers (Fig. 2a), increasing the degree of constraint from the harder α' as evidenced by the higher number of dislocations in β at the α'/β interface (Fig. 8d) which could locally increase the stress high enough to trigger slip in α'.

It is interesting to note that although the high YS in the ternary HYTA reduces the difference between YS and UTS, leading to smaller work hardening rates (Fig. 7g), its UE is actually higher as it takes longer to reach UTS. Further, the extremely heterogeneous microstructures give the ternary HYTA a wide range of hardness (Fig. 7a), ensuring deformation to take place at various locations rather than concentrated at one place. The long stage of slow work hardening implies that the deformation can be transferred harmonically between various structures, preventing localisation of deformation. It is worth noting that the higher yield stress of the ternary HYTA leads to a higher density of slip bands and dislocations after straining to 1.5% (Fig. 8b). This would increase the number of slip band intersections, enhancing work hardening in the β Ti-5553, as previously reported in a β Ti-Nb gum metal [38].

Journal Pre-proof

One of the mechanisms for deformation transfer between β and α' is β grain rotation, which has been observed in Figs. 8e-i. The changed orientations of β in the identified layer could not be attributed to twinning since SAEDPs did not show any evidence. It could not be a different grain formed during solidification either, since the TEM specimen was cut from one single prior β grain. One possibility is through grain rotation during plastic deformation, which could relieve stress from strain mismatch between α' and β at their interfaces. Rotation of β grains was observed during deformation of some monolithic β-phase Ti alloys, accomplished by kink banding [39, 40]. In the present work, however, the grain rotation was limited to the α'/β interface. Therefore, a new mechanism based on the restriction of deformation in β by α' is proposed, as illustrated in Fig. 12. Fig. 12a shows a single β crystal with two slip planes (red and blue dashed lines) subjected to tensile stressing. If there is no constraint, free glide is possible, creating steps along the slip planes (Fig. 12b). However, if one side of the β crystal is restricted by a rigid wall (Fig. 12c), e.g. an α' layer (Fig. 8e) which is reasonable since stress is not large enough to substantially deform it at the early stages of straining, the shearing forces F on a slip plane (green dashed line) would be balanced by the pair of shear forces F_W exerted by the rigid wall since no sliding as in Fig. 12b is allowed. The two pairs of the shear forces together create two clock-wise rotating torques on the two sides of the slip plane, which eventually force that part of the β crystal close to the interface to rotate (shaded blue in Fig. 12d). Although this simplified model considers only one slip band, it should be noted that a number of slip bands could be activated, causing rotation in various directions. In reality, the change in orientation would occur gradually, rather than suddenly as might be inferred in Fig. 12d. Within the newly formed bands of β, slip and SIMT can be operative, with the latter producing α'' (Fig. 12e, and observed in Figs. 8j and 9f), further relieving stress and accommodating strain. The boundary between the two β crystals with different orientations can act as an obstacle against dislocation movement, leading to pileup of dislocations and work hardening (Figs. 9f-g).

Journal Pre-proof

Journal Pre-proof

When strain is increased to 6.5%, more slip bands are formed and a large number of dislocations pile up at the α'/β interfaces (Fig. 9a), causing further work hardening. Another source of work hardening is due to a large number of α" plates formed in low β stability layers sandwiched between Ti-5553 (Fig. 9b) as a result of either SIMT or rapid cooling. These α" play an important role in obstructing dislocation slip, contributing to work hardening. The accumulation of dislocations behind these obstacles increases the forward stress at the head of pileups [41], eventually enabling slip bands to cut through α" and creating square-shaped α" (Fig. 9c), similar to our previous observations [17, 42].

Additionally, Fig. 9d shows steps at the α'/β interfaces, indicating that deformation is transferred from β to α' along the slip bands via either slip banding or twinning (Figs. 9e and f), depending on the composition and hardness of the α'. In general, twinning is more likely in the Ti alloys with lower contents of solute elements. Most of the α' plates observed here were rich in Al and V, and as reported previously [43, 44], Al reduces the likelihood of twinning in Ti. Indeed, significant twinning is only observed in a diluted Ti alloy layer (Fig. 9f) and these twins are mechanical since they are not present before straining and form at the dislocation pileups along slip bands in the neighbouring β layers. These mechanical twins of $\{10\bar{1}1\}$-type (inset, Fig. 9f) are normally activated at high temperature or when hcp-Ti is heavily deformed [45-47]. The latter must be the case here since the testing was done at room temperature and the TEM specimen was cut from a severely deformed area close to the necking zone.

In summary, the improved ductility in the ternary HYTA can be attributed to the following reasons. The newly added features such as additional α', diluted Ti regions at interfaces and pure Ti in the ternary HYTA have significantly increased the complexity and heterogeneity of the overall microstructure. This allows the deformation to transfer between microstructures more harmonically and activates new deformation mechanisms such as significant twinning in the hcp phases and stress

Journal Pre-proof

induced α" due to reduced β stability at interfaces, resulting in high work hardening and enhanced ductility. The increased amount of α' and decreased amount of β, as well as, refined layer structures in the ternary HYTA have led to more subtle differences in strength between different microstructure, producing a smooth curve without the stages in the binary alloy.

5. Conclusions

(1) A ternary HYTA was successfully produced by SLM, combining all three major types of Ti alloys (α CP Ti, α-β Ti-64 and β Ti-5553) and leading to a highly heterogeneous microstructure encompassing a wide variety of phases and structures that do not co-exist in conventional Ti alloys.

(2) The formation of such a complex microstructure from hybridisation of different alloys was strongly influenced by the distribution of the ingredient alloy particles, the Marangoni convection and diffusion of solute during melting, and microsegregation of solute during solidification. In particular, the ingredient alloys form layers of different thicknesses, depending on the size of the particle clusters of each alloy; the solute diffusion in the liquid state, affected by atomic mass and radius, resulted in altered compositions in layers next to the interface, giving rise to newly formed α-β alloys with different β stabilities from those of the ingredient alloys; internal cells formed in Ti-5553 as a result of microsegregation of mainly Mo owing to its partitioning behaviour during solidification.

(3) The ternary HYTA exhibited an excellent combination of high tensile strength (YS = 1000 MPa and UTS = 1100 MPa) and enhanced ductility (UE = ~15% and total elongation = ~20%), superior to conventional Ti alloys of various types. The good mechanical performance is attributed to the effective coordination between various components of the highly

Journal Pre-proof

heterogeneous microstructure, with all the possible deformation mechanisms including slip, twinning, SIMT and grain rotation activated and transferring smoothly between parts with a wide distribution of hardness (~4-6 GPa).

(4) Together with the binary HYTA reported earlier [3], the extraordinary tensile properties achieved in ternary HYTA serve to further demonstrate the potential of hybridisation of microstructures as a new strategy for future alloy development, applicable to all alloy systems.

Acknowledgements

We are grateful to Mr. Graham Hutchinson for conducting WDS analysis and to Mr. Daejung Kim for producing the binary powder and Fig. 3e. We appreciate the facilities and technical assistance provided by the Bio21 Advanced Microscopy Unit, and Melbourne TrACEES Platform (Trace Analysis for Chemical and Environmental Sciences) at the University of Melbourne and by RMMF (RMIT Microscopy and Microanalysis Facility) at RMIT University. The financial support by the Australian Research Council under DP190103557 and the University of Melbourne (ECRG2020) is acknowledged.

Journal Pre-proof

Data availability

The raw/processed data required to reproduce these findings cannot be shared at this time due to technical or time limitations.

Journal Pre-proof

References

[1] N. Fonstein, Advanced High Strength Sheet Steels, Springer, New York, 2015.

[2] S. Banerjee, P. Mukhopadhyay, Phase Transformations: Examples from Titanium and Zirconium Alloys, Elsevier, Oxford, 2010.

[3] A. Zafari, K. Xia, Superior titanium from hybridised microstructures – A new strategy for future alloys, Scr. Mater. 173 (2019) 61-65. https://doi.org/10.1016/j.scriptamat.2019.07.031.

[4] M. Marteleur, F. Sun, T. Gloriant, P. Vermaut, P. Jacques, F. Prima, On the design of new β-metastable titanium alloys with improved work hardening rate thanks to simultaneous TRIP and TWIP effects, Scr. Mater. 66 (2012) 749-752. https://doi.org/10.1016/j.scriptamat.2012.01.049

[5] J. Zhang, F. Sun, Z. Chen, Y. Yang, B. Shen, J. Li, F. Prima, Strong and ductile beta Ti–18Zr–13Mo alloy with multimodal twinning, Mater. Res. Lett. 7 (2019) 251-257. https://doi.org/10.1080/21663831.2019.1595763.

[6] C. de Formanoir, A. Brulard, S. Vivès, G. Martin, F. Prima, S. Michotte, E. Rivière, A. Dolimont, S. Godet, A strategy to improve the work-hardening behavior of Ti–6Al–4V parts produced by additive manufacturing, Mater. Res. Lett. 5 (2017) 201-208. https://doi.org/10.1080/21663831.2016.1245681.

[7] M. Fischer, D. Joguet, G. Robin, L. Peltier, P. Laheurte, In situ elaboration of a binary Ti–26Nb alloy by selective laser melting of elemental titanium and niobium mixed powders, Mater. Sci. Eng. C 62 (2016) 852-859.

[8] S.L. Sing, W.Y. Yeong, F.E. Wiria, Selective laser melting of titanium alloy with 50 wt% tantalum: Microstructure and mechanical properties, J. Alloys Compd. (2016) 461-470. https://doi.org/10.1016/j.ijrmhm.2018.08.006.

[9] R. Banerjee, S. Nag, S. Samuel, H.L. Fraser, Laser-deposited Ti-Nb-Zr-Ta orthopedic alloys, J. Biomed. Mater. Res. Part A 78 (2006) 298-305. https://doi.org/10.1002/jbm.a.30694.

[10] P. Barriobero-Vila, J. Gussone, A. Stark, N. Schell, J. Haubrich, G. Requena, Peritectic titanium alloys for 3D printing, Nat. Commun. 9 (2018) 3426. https://doi.org/10.1038/s41467-018-05819-9.

[11] M. Simonelli, N.T. Aboulkhair, P. Cohen, J.W. Murray, A.T. Clare, C. Tuck, R.J. Hague, A comparison of Ti-6Al-4V in-situ alloying in selective laser melting using simply-mixed and satellited powder blend feedstocks, J. Mater. Charact. 143 (2018) 118-126. https://doi.org/10.1016/j.matchar.2018.05.039.

[12] J.O. Hirschfelder, C.F. Curtiss, R.B. Bird, M.G. Mayer, Molecular Theory of Gases and Liquids, Wiley, New York, 1954.

[13] R. Davis, H. Flower, D. West, Martensitic transformations in Ti-Mo alloys, J. Mater. Sci. 14 (1979) 712-722. https://doi.org/10.1007/BF00772735.

[14] S. Banerjee, R. Krishnan, Martensitic transformation in zirconium-niobium alloys, Acta Metall. 19 (1971) 1317-1326. https://doi.org/10.1016/0001-6160(71)90068-X.

[15] D. Banerjee, K. Muraleedharan, J. Strudel, Substructure in titanium alloy martensite, Philos. Mag. A 77 (1998) 299-323. https://doi.org/10.1080/01418619808223754.

[16] H. Schwab, F. Palm, U. Kühn, J. Eckert, Microstructure and mechanical properties of the near-beta titanium alloy Ti-5553 processed by selective laser melting, Mater. Des. 105 (2016) 75-80. https://doi.org/10.1016/j.matdes.2016.04.103.

[17] A. Zafari, K. Xia, Stress induced martensitic transformation in metastable β Ti-5Al-5Mo-5V-3Cr alloy: Triggering stress and interaction with deformation bands, Mater. Sci. Eng. A 724 (2018) 75-79. https://doi.org/10.1016/j.msea.2018.03.070.

Journal Pre-proof

[18] P. Yuan, D. Gu, D. Dai, Particulate migration behavior and its mechanism during selective laser melting of TiC reinforced Al matrix nanocomposites, Mater. Design 82 (2015) 46-55. https://doi.org/10.1016/j.matdes.2015.05.041.
[19] M. Bermingham, S. McDonald, M. Dargusch, D. StJohn, Grain-refinement mechanisms in titanium alloys, J. Mater. Res. 23 (2008) 97-104. https://doi.org/10.1557/JMR.2008.0002.
[20] A. Mitchell, A. Kawakami, S. Cockcroft, Beta fleck and segregation in titanium alloy ingots, High Temp. Mater. Processes 25(2006) 337-349. https://doi.org/10.1515/HTMP.2006.25.5-6.337.
[21] A. Mitchell, Melting, casting and forging problems in titanium alloys, Mater. Science Eng. A 243 (1998) 257-262. https://doi.org/10.1016/S0921-5093(97)00810-1.
[22] X. Liu, G. Feng, Y. Zhou, Q. Fan, Macrosegregation and the underlying mechanism in Ti-6.5 Al-1.0 Cr-0.5 Fe-6.0 Mo-3.0 Sn-4.0 Zr alloy, Prog. Nat. Sci. 29 (2019) 224-230. https://doi.org/10.1016/j.pnsc.2019.02.006.
[23] B. Vrancken, L. Thijs, J.P. Kruth, J.B. Van-Humbeeck, Microstructure and mechanical properties of a novel β titanium metallic composite by selective laser melting, Acta Mater. 68 (2014) 150-158. https://doi.org/10.1016/j.actamat.2014.01.018.
[24] L. Facchini, E. Magalini, P. Robotti, A. Molinari, S. Höges, K. Wissenbach, Ductility of a Ti□6Al□4V alloy produced by selective laser melting of prealloyed powders, Rapid prototyp. J. 16 (2010) 450-459. https://doi.org/10.1108/13552541011083371.
[25] M.J. Donachie, Titanium: A Technical Guide, ASM International, Materials Park, OH, 2000.
[26] A. Zafari, K. Xia, High ductility in a fully martensitic microstructure: a paradox in a Ti alloy produced by selective laser melting, Mater. Res. Lett. 6 (2018) 627-633. https://doi.org/10.1080/21663831.2018.1525773.
[27] A. Zafari, M.R. Barati, K. Xia, Controlling martensitic decomposition during selective laser melting to achieve best ductility in high strength Ti-6Al-4V, Mater. Sci. Eng. A 744 (2019) 445-455. https://doi.org/10.1016/j.msea.2018.12.047.
[28] T. Voisin, N.P. Calta, S.A. Khairallah, J.-B. Forien, L. Balogh, R.W. Cunningham, A.D. Rollett, Y.M. Wang, Defects-dictated tensile properties of selective laser melted Ti-6Al-4V, Mater. Des. 158 (2018) 113-126. https://doi.org/10.1016/j.matdes.2018.08.004.
[29] J. Huang, Z. Wang, K. Xue, Cyclic deformation response and micromechanisms of Ti alloy Ti–5Al–5V–5Mo–3Cr–0.5Fe, Mater. Sci. Eng. A 528 (2011) 8723-8732. https://doi.org/10.1016/j.msea.2011.08.045.
[30] V. Opini, C.A.F. Salvador, K. Campo, E.S.N. Lopes, R. Chaves, R. Caram, α phase precipitation and mechanical properties of Nb-modified Ti-5553 alloy, Mater. Sci. Eng. A 670 (2016) 112-121. https://doi.org/10.1016/j.msea.2016.06.001.
[31] X.H. Min, K. Tsuzaki, S. Emura, K. Tsuchiya, Enhancement of uniform elongation in high strength Ti–Mo based alloys by combination of deformation modes, Mater. Sci. Eng. A 528 (2011) 4569-4578. https://doi.org/10.1016/j.msea.2011.02.071.
[32] X.H. Min, S. Emura, N. Sekido, T. Nishimura, K. Tsuchiya, K. Tsuzaki, Effects of Fe addition on tensile deformation mode and crevice corrosion resistance in Ti–15Mo alloy, Mater. Sci. Eng. A 527 (2010) 2693-2701. https://doi.org/10.1016/j.msea.2009.12.050.
[33] X.H. Min, S. Emura, T. Nishimura, K. Tsuchiya, K. Tsuzaki, Microstructure, tensile deformation mode and crevice corrosion resistance in Ti–10Mo–xFe alloys, Mater. Sci. Eng. A 527 (2010) 5499-5506. https://doi.org/10.1016/j.msea.2010.06.016.
[34] X. Ji, S. Emura, X. Min, K. Tsuchiya, Strain-rate effect on work-hardening behavior in β-type Ti-10Mo-1Fe alloy with TWIP effect, Mater. Sci. Eng. A 707 (2017) 701-707. https://doi.org/10.1016/j.msea.2017.09.055.

Journal Pre-proof

[35] W.L. Wang, X.L. Wang, W. Mei, J. Sun, Role of grain size in tensile behavior in twinning-induced plasticity β Ti-20V-2Nb-2Zr alloy, Mater. Charact. 120 (2016) 263-267. https://doi.org/10.1016/j.matchar.2016.09.016.

[36] W. Wang, X. Zhang, J. Sun, Phase stability and tensile behavior of metastable β Ti-V-Fe and Ti-V-Fe-Al alloys, Mater. Charact. 142 (2018) 398-405. https://doi.org/10.1016/j.matchar.2018.06.008.

[37] C. Brozek, F. Sun, P. Vermaut, Y. Millet, A. Lenain, D. Embury, P.J. Jacques, F. Prima, A β-titanium alloy with extra high strain-hardening rate: Design and mechanical properties, Scr. Mater. 114 (2016) 60-64. https://doi.org/10.1016/j.scriptamat.2015.11.020.

[38] M.J. Lai, C.C. Tasan, D. Raabe, Deformation mechanism of ω-enriched Ti–Nb-based gum metal: Dislocation channeling and deformation induced ω–β transformation, Acta Mater. 100 (2015) 290-300. https://doi.org/10.1016/j.actamat.2015.08.047.

[39] Y. Yang, S. Wu, G. Li, Y. Li, Y. Lu, K. Yang, P. Ge, Evolution of deformation mechanisms of Ti–22.4 Nb–0.73 Ta–2Zr–1.34 O alloy during straining, Acta Mater. 58 (2010) 2778-2787. https://doi.org/10.1016/j.actamat.2010.01.015.

[40] T. Furuta, S. Kuramoto, J. Hwang, K. Nishino, T. Saito, Elastic deformation behavior of multi-functional Ti–Nb–Ta–Zr–O alloys, Mater. Trans. 46 (2005) 3001-3007. https://doi.org/10.2320/matertrans.46.3001.

[41] Y. Zhu, X. Wu, Perspective on hetero-deformation induced (HDI) hardening and back stress, Mater. Res. Lett. 7 (2019) 393-398. https://doi.org/10.1080/21663831.2019.1616331.

[42] A. Zafari, X.S. Wei, W. Xu, K. Xia, Formation of nanocrystalline β structure in metastable beta Ti alloy during high pressure torsion: The role played by stress induced martensitic transformation, Acta Mater. 97 (2015) 146-155. doi: 10.1016/j.actamat.2015.06.042.

[43] J.C. Williams, R.G. Baggerly, N.E. Paton, Deformation behavior of HCP Ti-Al alloy single crystals, Metall. Mater. Trans. A 33 (2002) 837-850. https://doi.org/10.1007/s11661-002-0153-y.

[44] H. Li, D. Mason, Y. Yang, T. Bieler, M. Crimp, C. Boehlert, Comparison of the deformation behaviour of commercially pure titanium and Ti–5Al–2.5 Sn (wt.%) at 296 and 728 K, Philos. Mag. 93 (2013) 2875-2895. https://doi.org/10.1080/14786435.2013.791752.

[45] N.E. Paton, W. Backofen, Plastic deformation of titanium at elevated temperatures, Metall. Trans. 1 (1970) 2839-2847. https://doi.org/10.1007/BF03037822.

[46] Y. Li, Y. Chen, J.C. Walmsley, R. Mathinsen, S. Dumoulin, H.J. Roven, Faceted interfacial structure of $\{10\bar{1}1\}$ twins in Ti formed during equal channel angular pressing, Scr. Mater. 62 (2010) 443-446. https://doi.org/10.1016/j.scriptamat.2009.11.039.

[47] A. Serra, R. Pond, D. Bacon, Computer simulation of the structure and mobility of twinning disclocations in hcp metals, Acta Metall. Mater. 39 (1991) 1469-1480. https://doi.org/10.1016/0956-7151(91)90232-P.

[48] H. Attar, M. Calin, L.C. Zhang, S. Scudino, J. Eckert, Manufacture by selective laser melting and mechanical behavior of commercially pure titanium, Mater. Sci. Eng. A 593 (2014) 170-177. https://doi.org/10.1016/j.msea.2013.11.038.

Journal Pre-proof

Figure Captions

Fig. 1 (a) EDS map for Mo of the as-mixed binary powder and (b) the distribution of Ti-64 (blue) and Ti-5553 (red) particles constructed from (a), showing clusters of ~100-200 μm for each alloy (selectively circled by dashed lines). EDS maps for (c) Ti, (d) Al and (e) Mo of the as-mixed ternary powder and (f) the distribution of CP Ti (yellow), Ti-64 (blue) and Ti-5553 (red), showing mostly clusters much smaller than 100 μm, although there are still some coarser ones (circled).

Fig. 2 (a) SEM in the ternary HYTA, showing prior β columns (selective white dotted lines) as well as dark and bright layers in the melt pool (selective yellow dashed lines) with the former dominated by α' and the latter by β. (b-g) WDS maps for Ti, Al, V, Mo, Cr and Fe, respectively, and (h) the distribution of CP Ti (yellow), Ti-64 (blue), Ti-5553 (red) and regions with compositions altered from the ingredient alloys (black) constructed from the elemental maps.

Fig. 3 (a-b) Thick layers with the original compositions of the ingredient alloys, and the boundaries of Ti-5553 (yellow arrowed) with altered compositions of low β stability leading to formation of needle-shaped martensite (inset in b). (c) Thin layers of original Ti-5553 completely transformed into martensitic α-β Ti with low β stability. (d) Isolated regions of single phase acicular α' with compositions different from those of the ingredient alloys. (e) Binary HYTA, showing thick layers of Ti-64 and Ti-5553 with some melt pools (selective dotted lines) consisting entirely of Ti-64 or Ti-5553. Point WDS/EDS analysis was performed at Points 1-9 with corresponding compositions listed in Table 2.

Fig. 4 TEM in a composition-altered α-β Ti region in the ternary HYTA, showing (a) acicular martensitic α' with substructural twins formed mainly in large plates (arrowed); (b)

Journal Pre-proof

SAEDP from the circled area in (a), indicating the twinning plane of $(0\bar{1}1\bar{1})_{MT}$ with M and T standing for martensite and twin, respectively; (c–d) substructural dislocations in α' plates (selectively arrowed); (e) stacking domains.

Fig. 5 (a) SEM in the boundary region between Ti-5553 and CP Ti (original interface indicated by the dashed line) in the ternary HYTA and corresponding EDS maps for Ti, Al, V and Mo, showing altered compositions from the original ones. (b-h) TEM in such a boundary area, showing (b) four zones of *A*-*D*, with *A* identified as Ti-5553 and *D* CP Ti. (c) SAEDP in zone A, identifying the β structure. (d) DF TEM from $(110)_{\beta}$ in (c). (e) Substructural dislocations in zone *D* (selectively arrowed). (f) SAEDP from zone *B*, detecting α'' twinned on $(1\bar{1}1)$. (g) SAEDP of α' plates in zone *C*. (h) STEM-EDS elemental maps from the framed area in (b).

Fig. 6 SEM in (a) the ternary HYTA, showing internal cells in Ti-5553, and (b) the as-SLM Ti-5553, showing the melt pool boundaries and cells inside. (c–d) APT in the as-SLM Ti-5553, showing single element atom maps from (c) a melt pool and (d) a melt pool boundary. (e) Variation of concentrations of solute elements from the melt pool boundary (distance 0) towards inside the melt pool, showing a reduction in Mo from ~6 at.% in the boundary to < 4 at.% inside the melt pool but little change in other elements.

Fig. 7 (a) Hardness map produced from nanoindentation on an area of 70 × 300 μm^2 along the build direction. (b-d) WDS maps for Ti, Al and Mo, respectively, collected from the same area. (e) The distributions of Ti-64 (blue), Ti-5553 (red), CP Ti (yellow) and regions with altered compositions (black) constructed from (b–d). White points in white contours have hardness > 5.2 GPa and green ones < 4.5 GPa corresponding to areas dominated by acicular α' rich in solute elements (e.g. Ti-64) and those largely free of

Journal Pre-proof

acicular α' (e.g. Ti-5553 or CP Ti), respectively. (f) Engineering tensile stress-strain curves and derived tensile properties for ternary and binary HYTAs as well as monolithic Ti-64 [26], Ti-5553 [3] and CP Ti (converted to engineering values) [48]. (g) The work hardening rate ($d\sigma/d\epsilon$) as a function of true strain (ϵ) for the binary and ternary HYTAs, showing much higher rates for the binary HYTA at $\epsilon > 5\%$.

Fig. 8 (a) TEM in the binary HYTA strained to 1.5%, showing a small number of slip bands. (b-j) TEM in the ternary HYTA strained to 1.5%: (b) a higher density of slip bands than that in (a); (c) STEM-HAADF, showing lens-shaped martensitic plates identified as α'' using SAEDP (inset) from the circled area (with weak diffractions of ω_{ath}); (d) an α'/β interface (dashed line) with dislocations generated in both α' and β (yellow triangles); (e) another α'/β interface, showing a β stripe between the dashed lines; (f-h) SAEDPs from *f*, *g*, and *h* circled in (e), respectively, showing extra diffraction spots (pointed by triangles) in (g) when comparing to (f), which form the same diffraction pattern (solid lines) as that from area *h* (h); (i) DF TEM from the circled spot in (g); (j) BF TEM (left) of a lens shaped martensitic plate in area *h* detected as α'' using the SAEDP from the circled area (inset) and DF TEM (right).

Fig. 9 (a-c) TEM in the ternary HYTA strained to 6.5%, showing (a) a high number of slip bands in β (Ti-5553) and dislocation pileups at the α'/β interface (right magnified from the framed area), (b) a stripe of α'' plates sandwiched between two β Ti-5553 regions and dislocation pileups at their interfaces delineated by dashed lines (right magnified from the framed area), and (c) DF TEM for α'', showing square shapes cut by slip bands (dashed lines). (d-g) TEM in the ternary HYTA strained until fracture, showing (d) steps created by β Ti-5553 slip bands (yellow dotted lines) in the β/α' interfaces (dashed lines), (e) penetration of the steps from β to α' via slip banding (arrowed) in the latter, (f)

Journal Pre-proof

dislocation pileups and twinning on $(10\bar{1}1)_{MT}$, identified by SAEDP (inset), at β/α' and β/diluted-Ti interfaces (white dashed-lines), and dislocation pileup in the boundary of two β regions (red dotted line), and (g) STEM-HAADF in the area surrounding the red dotted-line in (f).

Fig. 10 Schematics of the formation of final microstructures in HYTA. Column 1: Possible distributions of Ti-64 (blue) and Ti-5553 (red) powders in the binary HYTA (a1-c1), and the distribution of Ti-64, Ti-5553 and CP-Ti (yellow) in the ternary HYTA (d1) in the melt pool before melting. Column 2: The corresponding alloy distribution in the melt pool after melting, as formed by Marangoni convection (illustrated at the bottom), showing layers of Ti-64 and Ti-5553 (a2), single occupation by either Ti-64 (b2) or Ti-5553 (c2) in the binary HYTA, and much thinner layers of the ingredient alloys in the ternary HYTA (d2) some of which was altered to new compositions (orange). Column 3: Formation of prior β columns immediately after solidification. White lines are prior β grain boundaries and solid black lines internal cell boundaries. Column 4: Solid state transformations after quenching to low temperatures, creating acicular martensitic α' in blue (Ti-64) and orange (newly formed α-β alloys). The β structure of Ti-5553 is preserved while CP-Ti undergoes β to massive martensitic α' transformation.

Fig. 11 (a) Schematic phase diagram, showing the classes of α, α-β (shaded) and β alloys with the positions of the ingredient alloys. Alloy 1 represents a newly formed alloy from interaction between the ingredient alloys with a composition close to the α-β/β boundary (black dashed line), and Alloy 2 another new alloy containing much lower amount of β stabilising elements. (b) Diffusion coefficient of a solute element in a binary system Ti-*x* (*x* =Al, V, Cr or Mo) in the temperature range of 1600-2000 °C (i.e. in liquid) calculated using the property diagram module of Thermo-Calc (commercial software

Journal Pre-proof

based on the CALPHAD method) by coupling thermodynamic database for Ti alloys and TCTI2 with MOBTI3.

Fig. 12 (a) Schematic of a β single crystal with no constraint subjected to a tensile stress (σ) and (b) formation of steps along slip planes (blue and red dashed lines) owing to free glide. (c) Schematic of a β single crystal restricted by a rigid wall (e.g. a hard α' layer) subjected to σ, leading to the shear forces F on a slip plane (green dashed line) and resisting forces F_W exerted on AB and BC in opposite directions, creating F/F_W force couples and clockwise torques (black arrows). (d) Rotation of the crystal next to the rigid wall (shaded blue). (e) Activation of dislocation slip and SIMT (creating martensitic α") in the rotated region.

Journal Pre-proof

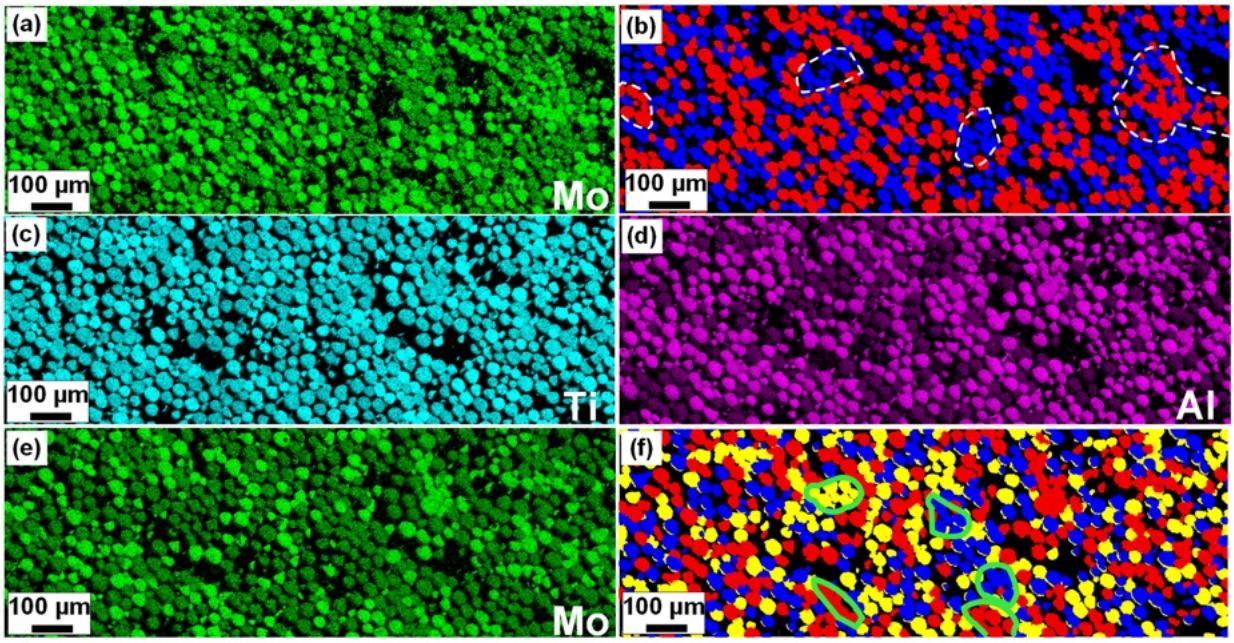

Fig. 1 (a) EDS map for Mo of the as-mixed binary powder and (b) the distribution of Ti-64 (blue) and Ti-5553 (red) particles constructed from (a), showing clusters of ~100-200 μm for each alloy (selectively circled by dashed lines). EDS maps for (c) Ti, (d) Al and (e) Mo of the as-mixed ternary powder and (f) the distribution of CP Ti (yellow), Ti-64 (blue) and Ti-5553 (red), showing mostly clusters much smaller than 100 μm, although there are still some coarser ones (circled).

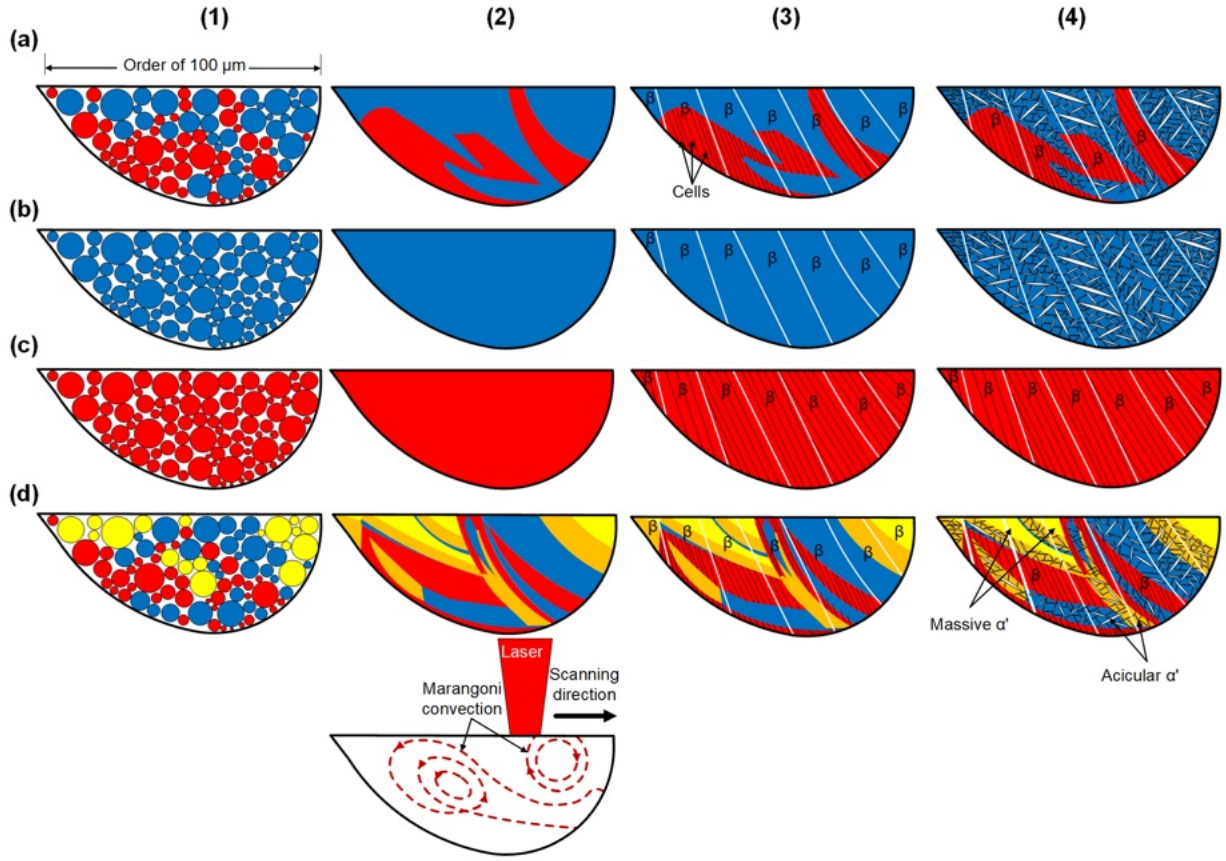

Fig. 10 Schematics of the formation of final microstructures in HYTA. Column 1: Possible distributions of Ti-64 (blue) and Ti-5553 (red) powders in the binary HYTA (a1-c1), and the distribution of Ti-64, Ti-5553 and CP-Ti (yellow) in the ternary HYTA (d1) in the melt pool before melting. Column 2: The corresponding alloy distribution in the melt pool after melting, as formed by Marangoni convection (illustrated at the bottom), showing layers of Ti-64 and Ti-5553 (a2), single occupation by either Ti-64 (b2) or Ti-5553 (c2) in the binary HYTA, and much thinner layers of the ingredient alloys in the ternary HYTA (d2) some of which was altered to new compositions (orange). Column 3: Formation of prior β columns immediately after solidification. White lines are prior β grain boundaries and solid black lines internal cell boundaries. Column 4: Solid state transformations after quenching to low temperatures, creating acicular martensitic α' in blue (Ti-64) and orange (newly formed α-β alloys). The β structure of Ti-5553 is preserved while CP-Ti undergoes β to massive martensitic α' transformation.

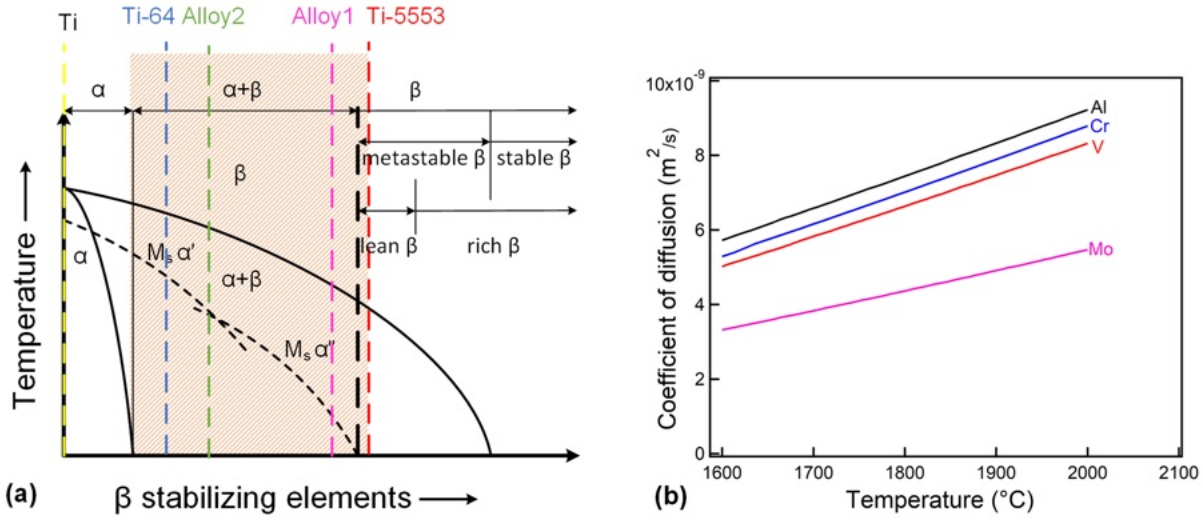

Fig. 11 (a) Schematic phase diagram, showing the classes of α, α-β (shaded) and β alloys with the positions of the ingredient alloys. Alloy 1 represents a newly formed alloy from interaction between the ingredient alloys with a composition close to the α-β/β boundary (black dashed line), and Alloy 2 another new alloy containing much lower amount of β stabilising elements. (b) Diffusion coefficient of a solute element in a binary system Ti-*x* (*x* =Al, V, Cr or Mo) in the temperature range of 1600-2000 °C (i.e. in liquid) calculated using the property diagram module of Thermo-Calc (commercial software based on the CALPHAD method) by coupling thermodynamic database for Ti alloys and TCTI2 with MOBTI3.

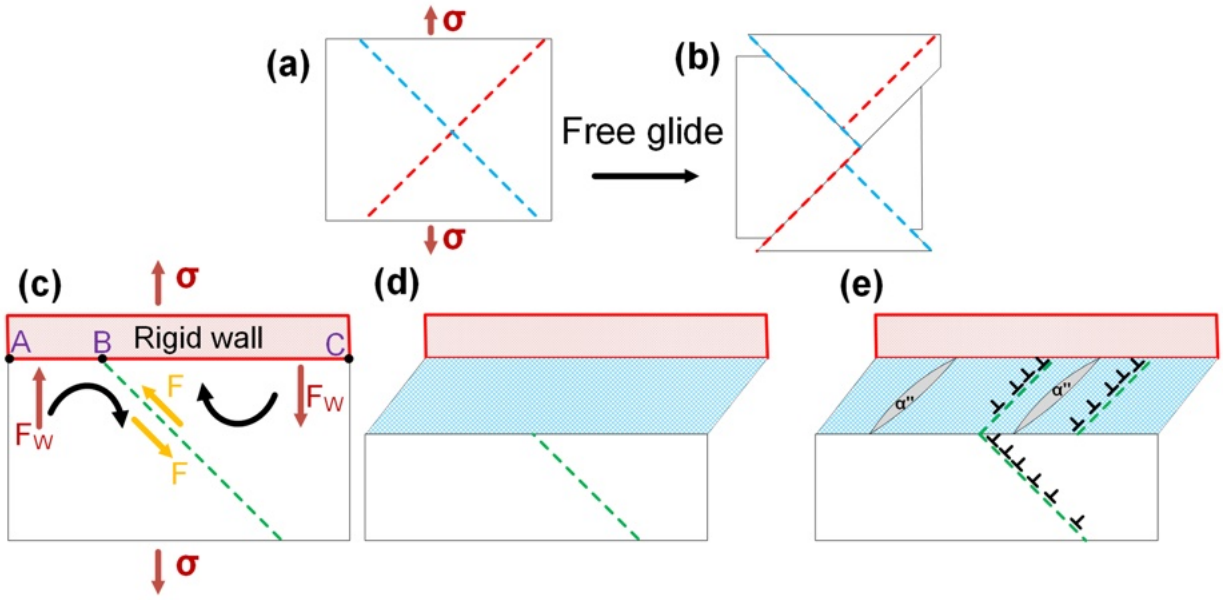

Fig. 12 (a) Schematic of a β single crystal with no constraint subjected to a tensile stress (σ) and (b) formation of steps along slip planes (blue and red dashed lines) owing to free glide. (c) Schematic of a β single crystal restricted by a rigid wall (e.g. a hard α' layer) subjected to σ, leading to the shear forces F on a slip plane (green dashed line) and resisting forces F_W exerted on AB and BC in opposite directions, creating F/F_W force couples and clockwise torques (black arrows). (d) Rotation of the crystal next to the rigid wall (shaded blue). (e) Activation of dislocation slip and SIMT (creating martensitic α'') in the rotated region.

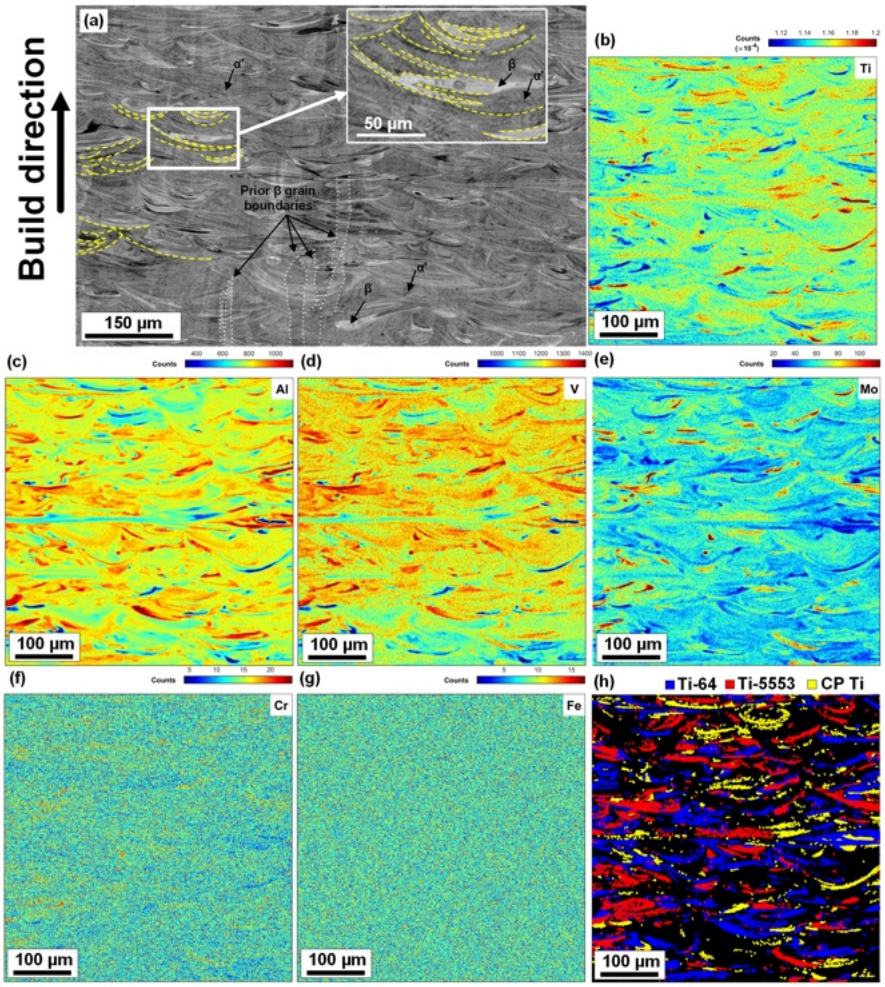

Fig. 2 (a) SEM in the ternary HYTA, showing prior β columns (selective white dotted lines) as well as dark and bright layers in the melt pool (selective yellow dashed lines) with the former dominated by α' and the latter by β. (b-g) WDS maps for Ti, Al, V, Mo, Cr and Fe, respectively, and (h) the distribution of CP Ti (yellow), Ti-64 (blue), Ti-5553 (red) and regions with compositions altered from the ingredient alloys (black) constructed from the elemental maps.

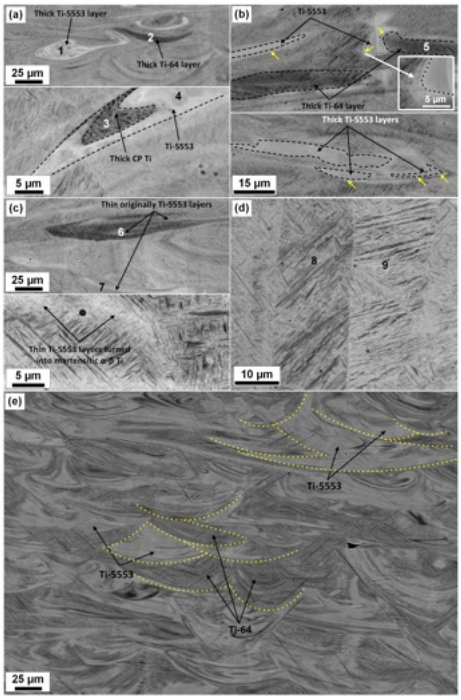

Fig. 3 (a-b) Thick layers with the original compositions of the ingredient alloys, and the boundaries of Ti-5553 (yellow arrowed) with altered compositions of low β stability leading to formation of needle-shaped martensite (inset in b). (c) Thin layers of original Ti-5553 completely transformed into martensitic α-β Ti with low β stability. (d) Isolated regions of single phase acicular α' with compositions different from those of the ingredient alloys. (e) Binary HYTA, showing thick layers of Ti-64 and Ti-5553 with some melt pools (selective dotted lines) consisting entirely of Ti-64 or Ti-5553. Point WDS/EDS analysis was performed at Points 1-9 with corresponding compositions listed in Table 2.

Journal Pre-proof

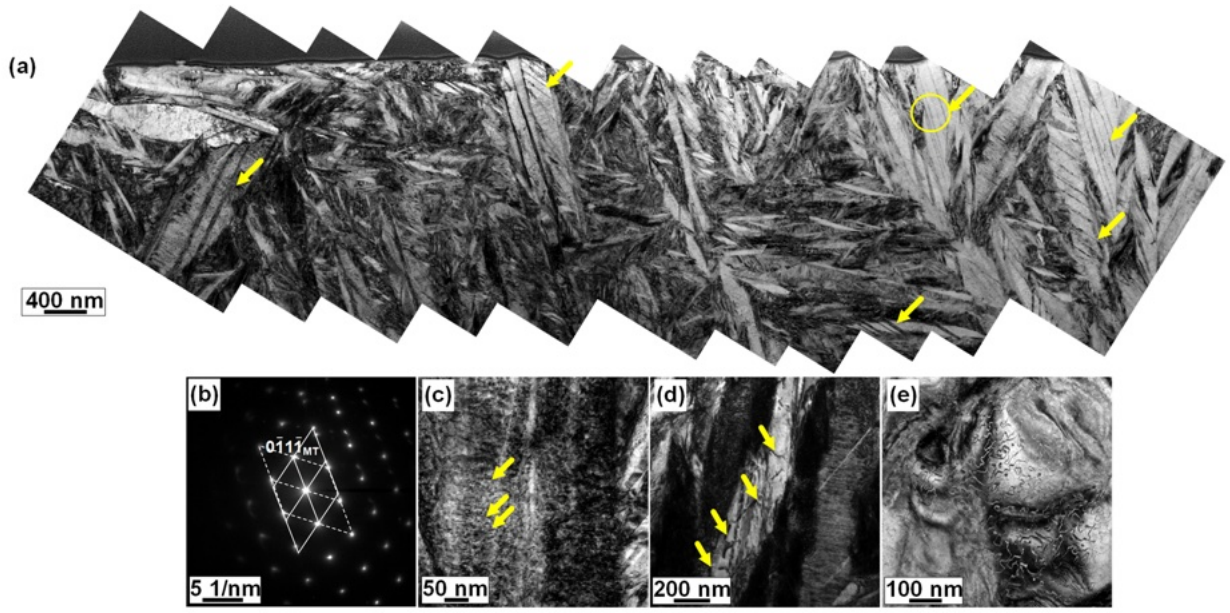

Fig. 4 TEM in a composition-altered α-β Ti region in the ternary HYTA, showing (a) acicular martensitic α' with substructural twins formed mainly in large plates (arrowed); (b) SAEDP from the circled area in (a), indicating the twinning plane of $(0\text{-}11\text{-}1)_{MT}$ with M and T standing for martensite and twin, respectively; (c–d) substructural dislocations in α' plates (selectively arrowed); (e) stacking domains.

Journal

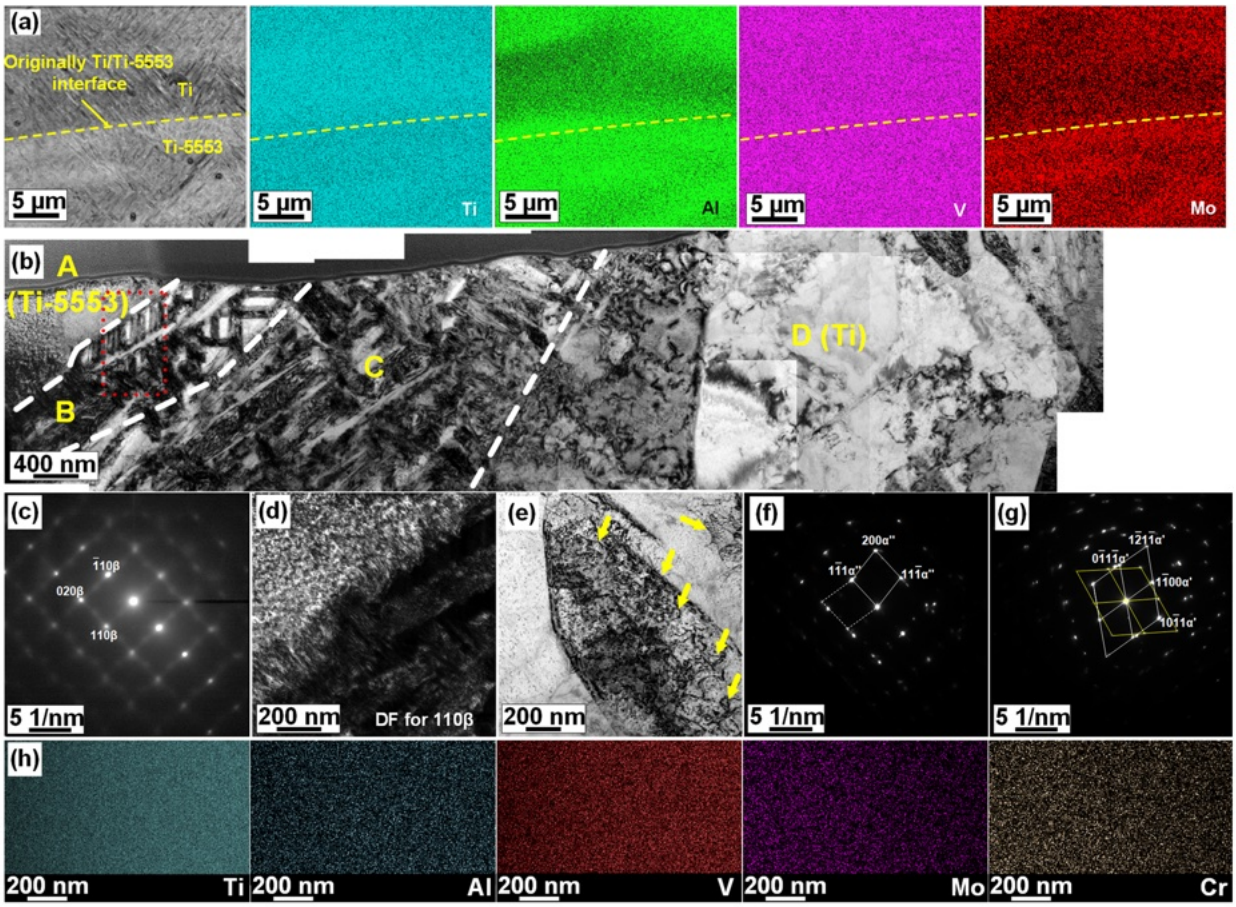

Fig. 5 (a) SEM in the boundary region between Ti-5553 and CP Ti (original interface indicated by the dashed line) in the ternary HYTA and corresponding EDS maps for Ti, Al, V and Mo, showing altered compositions from the original ones. (b-h) TEM in such a boundary area, showing (b) four zones of *A*-*D*, with *A* identified as Ti-5553 and *D* CP Ti. (c) SAEDP in zone A, identifying the β structure. (d) DF TEM from $(110)_\beta$ in (c). (e) Substructural dislocations in zone *D* (selectively arrowed). (f) SAEDP from zone *B*, detecting α'' twinned on (1-11). (g) SAEDP of α' plates in zone *C*. (h) STEM-EDS elemental maps from the framed area in (b).

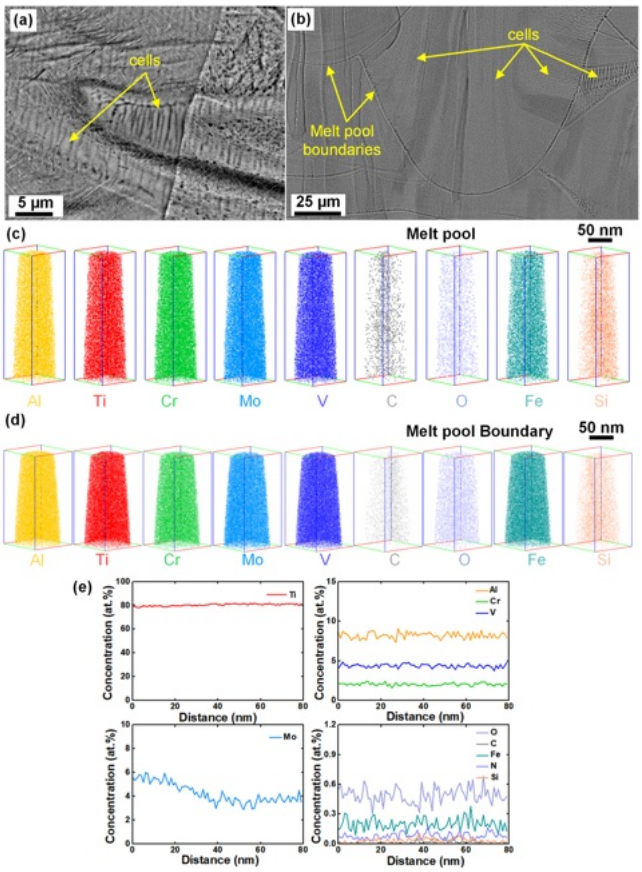

Fig. 6 SEM in (a) the ternary HYTA, showing internal cells in Ti-5553, and (b) the as-SLM Ti-5553, showing the melt pool boundaries and cells inside. (c–d) APT in the as-SLM Ti-5553, showing single element atom maps from (c) a melt pool and (d) a melt pool boundary. (e) Variation of concentrations of solute elements from the melt pool boundary (distance 0) towards inside the melt pool, showing a reduction in Mo from ~6 at.% in the boundary to < 4 at.% inside the melt pool but little change in other elements.

Journal Pre-proof

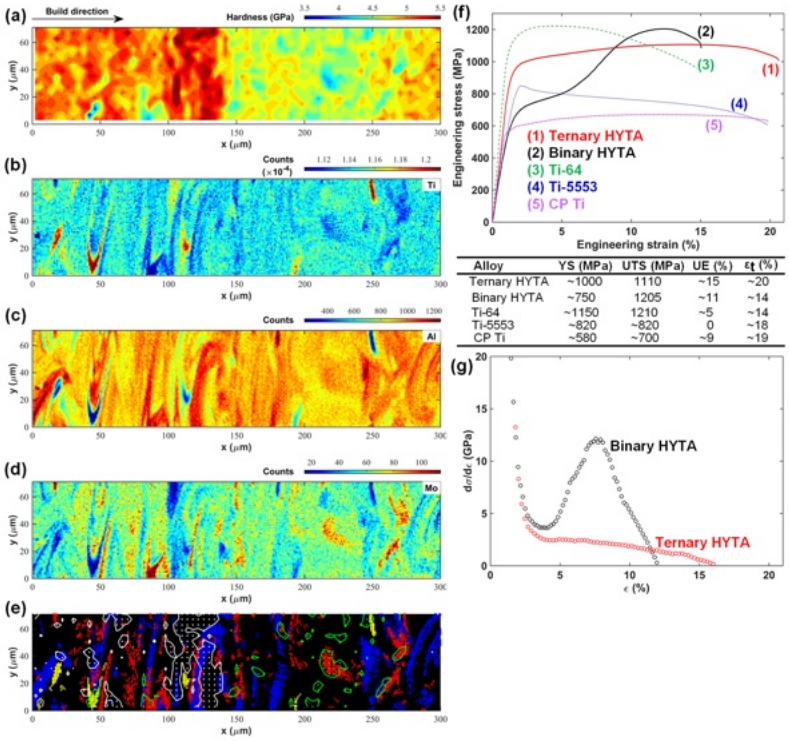

Alloy	YS (MPa)	UTS (MPa)	UE (%)	εt (%)
Ternary HYTA	~1000	1110	~15	~20
Binary HYTA	~750	1205	~11	~14
Ti-64	~1150	1210	~5	~14
Ti-5553	~820	~820	0	~18
CP Ti	~580	~700	~9	~19

Fig. 7 (a) Hardness map produced from nanoindentation on an area of 70 × 300 μm^2 along the build direction. (b-d) WDS maps for Ti, Al and Mo, respectively, collected from the same area. (e) The distributions of Ti-64 (blue), Ti-5553 (red), CP Ti (yellow) and regions with altered compositions (black) constructed from (b–d). White points in white contours have hardness > 5.2 GPa and green ones < 4.5 GPa corresponding to areas dominated by acicular α' rich in solute elements (e.g. Ti-64) and those largely free of acicular α' (e.g. Ti-5553 or CP Ti), respectively. (f) Engineering tensile stress-strain curves and derived tensile properties for ternary and binary HYTAs as well as monolithic Ti-64 [26], Ti-5553 [3] and CP Ti (converted to engineering values) [48]. (g) The work hardening rate ($d\sigma/d\epsilon$) as a function of true strain (ϵ) for the binary and ternary HYTAs, showing much higher rates for the binary HYTA at $\epsilon > 5\%$.

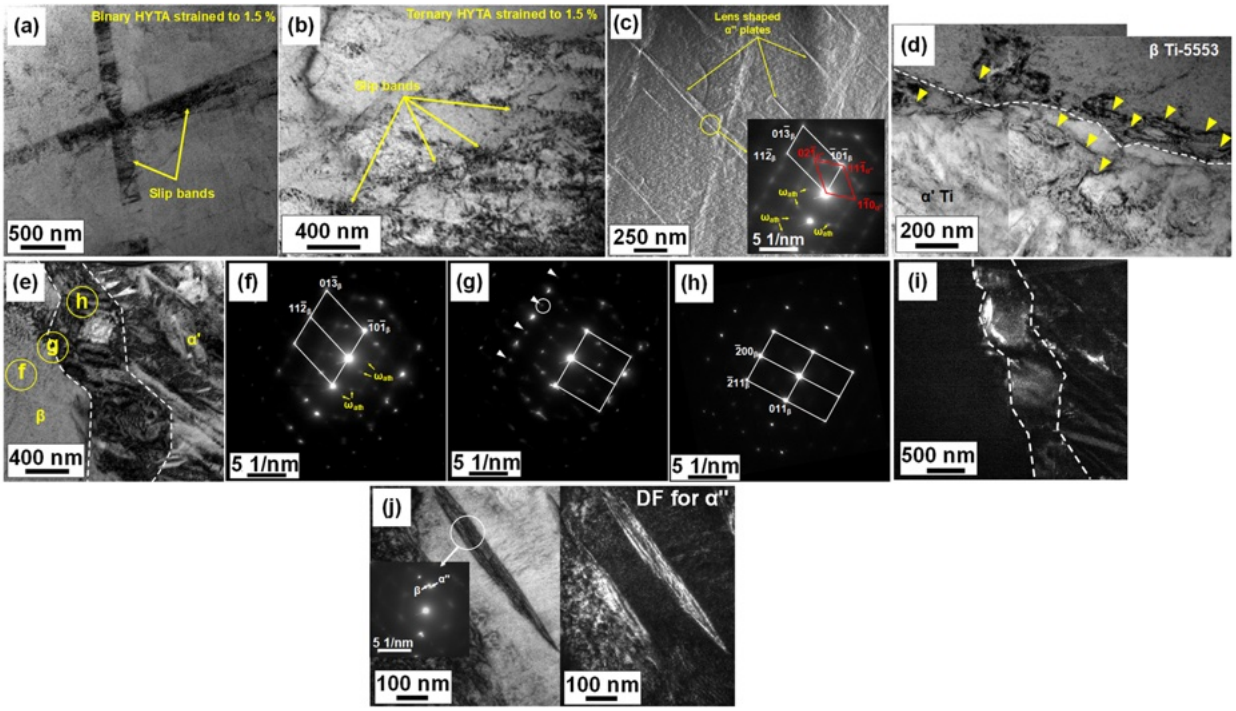

Fig. 8 (a) TEM in the binary HYTA strained to 1.5%, showing a small number of slip bands. (b-j) TEM in the ternary HYTA strained to 1.5%: (b) a higher density of slip bands than that in (a); (c) STEM-HAADF, showing lens-shaped martensitic plates identified as α'' using SAEDP (inset) from the circled area (with weak diffractions of ω_{ath}); (d) an α'/β interface (dashed line) with dislocations generated in both α' and β (yellow triangles); (e) another α'/β interface, showing a β stripe between the dashed lines; (f-h) SAEDPs from *f*, *g*, and *h* circled in (e), respectively, showing extra diffraction spots (pointed by triangles) in (g) when comparing to (f), which form the same diffraction pattern (solid lines) as that from area *h* (h); (i) DF TEM from the circled spot in (g); (j) BF TEM (left) of a lens shaped martensitic plate in area *h* detected as α'' using the SAEDP from the circled area (inset) and DF TEM (right).

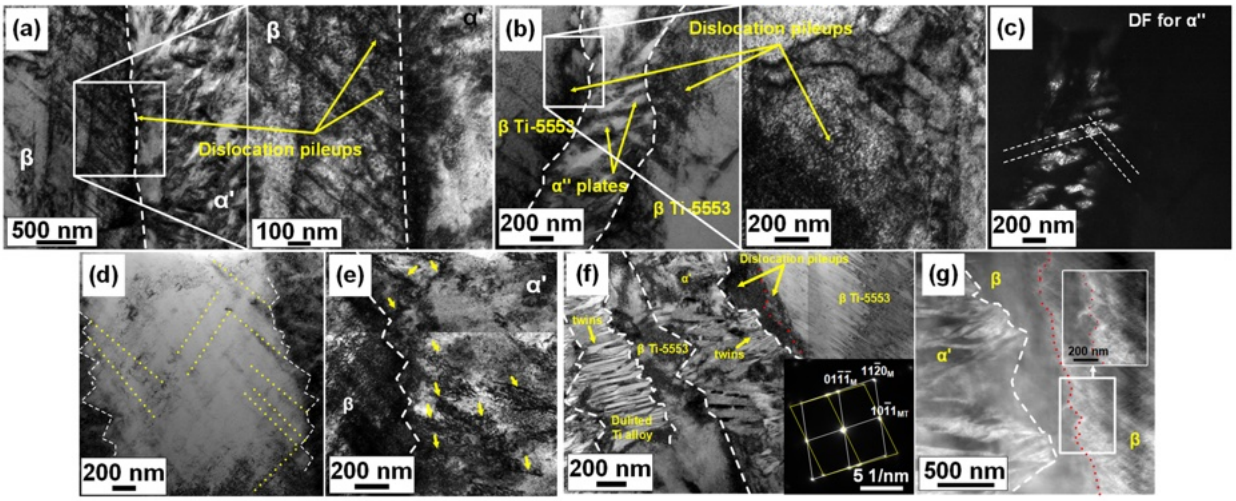

Fig. 9 (a-c) TEM in the ternary HYTA strained to 6.5%, showing (a) a high number of slip bands in β (Ti-5553) and dislocation pileups at the α'/β interface (right magnified from the framed area), (b) a stripe of α'' plates sandwiched between two β Ti-5553 regions and dislocation pileups at their interfaces delineated by dashed lines (right magnified from the framed area), and (c) DF TEM for α'', showing square shapes cut by slip bands (dashed lines). (d-g) TEM in the ternary HYTA strained until fracture, showing (d) steps created by β Ti-5553 slip bands (yellow dotted lines) in the β/α' interfaces (dashed lines), (e) penetration of the steps from β to α' via slip banding (arrowed) in the latter, (f) dislocation pileups and twinning on $(10\text{-}11)_{MT}$, identified by SAEDP (inset), at β/α' and β/diluted-Ti interfaces (white dashed-lines), and dislocation pileup in the boundary of two β regions (red dotted line), and (g) STEM-HAADF in the area surrounding the red dotted-line in (f).

Journal

Journal Pre-proof

Declaration of interests

☒ The authors declare that they have no known competing financial interests or personal relationships that could have appeared to influence the work reported in this paper.

☐The authors declare the following financial interests/personal relationships which may be considered as potential competing interests:

Journal Pre-proof